# Toward Transparency and Consistency: An Open-Source Optics Parameterization for Clouds and Precipitation

**Jing Feng[1], Raymond Menzel[2], and David Paynter[2]**

[1]Atmospheric and Oceanic Sciences Program, Princeton University, Princeton, NJ, USA, [2]Geophysical Fluid Dynamics Laboratory, Princeton, NJ, USA

**Abstract** In this study, a new open-source package for cloud and precipitation modeling is introduced. Based on Mie theory and existing ice crystal data sets, the scheme generates optical properties for user-defined gas bands, particle size distribution, and crystal habits, ensuring continuity across wide spectral bands and from small particles (clouds) to large particles (precipitation). Compared with existing schemes in GFDL's AM4-MG2, it reduces shortwave reflection of liquid clouds at the top of the atmosphere (TOA) by $1.50 \, \text{Wm}^{-2}$ and increases that of ice clouds by $1.62 \, \text{Wm}^{-2}$, based on offline radiative calculations. Using the new scheme, we find that cloud radiative effects are sensitive to microphysics variables such as particle size and habit, which affect the effective radius. Systematic flux biases may arise if the effective radius is not fully predicted in microphysics due to predefined size and habit distributions. We show that assuming spherical ice crystals underestimates ice-cloud radiative effects by $3.20 \, \text{Wm}^{-2}$ in the longwave TOA and $2.76 \, \text{Wm}^{-2}$ in the shortwave TOA. These biases can be addressed by improving the effective radius approximation with a volume-to-radius ratio derived from in-situ measurements. Combining these findings, we propose that climate models use a set of optics parameterizations for each hydrometeor type while adequently accounting for radiation effects caused by size and habit distributions. Uncertainties due to this simplification are evaluated. This study offers a consistent and physically based representation of radiative processes of clouds and precipitation in weather and climate simulations.

**Plain Language Summary** Clouds play a vital role in Earth's energy balance, as they both reflect sunlight and trap heat. A cloud optics parameterization describes how cloud particles interact with radiation and is an essential part of climate and weather models. In this study, we introduce a new parameterization that unifies the treatment of clouds (small particles) and precipitation (large particles) for both liquid and ice. Our parameterization is generated using an open-source code at user-selected wavelength ranges, and it interacts with microphysics schemes through the effective radius. Because the effective radius strongly depends on particle size and shape—factors not always fully resolved by models—we developed an approximation that converts the volume-mean radius to the effective radius in such scenarios. This approach simplifies the implementation in other models and improves transparency and traceability of climate models.

## 1. Introduction

Clouds are known to be an important radiative driver of Earth's climate system and lead to compensating effects on radiation fluxes. They attenuate the upwelling longwave (LW) fluxes at the top-of-atmosphere (TOA) and the downwelling shortwave (SW) fluxes at the surface, while concurrently enhancing the downwelling LW fluxes at the surface and the upwelling SW fluxes at the TOA. It is one of the largest sources of uncertainties in the representation of current climate (Wild, 2020) and the projected warming (Zelinka et al., 2020).

In general circulation models (GCMs), radiation fluxes in cloudy grids are calculated by radiation schemes that combine cloud optics with gas and aerosol optics and conduct radiative transfer calculations. In this process, cloud optical properties are inferred from parameterization files that approximate mass extinction coefficient, single-scattering-albedo, and asymmetry factor, as a function of effective radius at a set of radiation bands. Even given identical conditions in clouds, surface, and atmosphere, these cloud optical properties can still have great impacts on cloud radiation effects (CRE).

Decades of studies have greatly advanced optics parameterizations of water condensate in GCMs. With the well-established Mie theory, previous studies have developed schemes for liquid clouds (Chou et al., 1999; Hu &

Stamnes, 1993; Slingo, 1989) and raindrops (Fu et al., 1995; Savijärvi, 1997; Savijärvi & Räisänen, 1998), assuming spherical shape. The parameterization of ice clouds is more complex due to the crystal habit, which is associated with differences in density, geometrical cross-section, surface roughness, orientation, and therefore extinction cross-section and scattering phase function of individual particles (A. J. Baran, 2009; Takano & Liou, 1989; van Diedenhoven et al., 2014). Ebert and Curry (1992), Fu and Liou (1993), and Fu (1996) have developed ice cloud schemes based on optical properties of hexagonal ice crystals computed from a geometric ray-tracing program (Takano & Liou, 1989). The ice scattering properties are found to be sensitive to crystal shapes (Takano & Liou, 1995) and parameterizations for various crystal shapes have been developed (Kristjánsson et al., 1999; McFarquhar et al., 2002; Wyser & Yang, 1998). P. Yang et al. (2008) further elucidates that the surface roughness of ice crystals is important. Optical properties for different crystal habits have been developed (Ding et al., 2017; Eriksson et al., 2018; Kleanthous et al., 2024; Macke, 1993; Takano & Liou, 1989; P. Yang et al., 2000, 2013). These optical properties have been used to build numerical parameterizations (A. J. Baran & Labonnote, 2007; A. J. Baran, Cotton, et al., 2014; Edwards et al., 2007; Ebert & Curry, 1992; Fu & Liou, 1993; A. Geer & Baordo, 2014; A. J. Geer et al., 2021; Kristjánsson et al., 1999; Key et al., 2002; Ren et al., 2023; Sieron et al., 2018; Yi et al., 2013, …) with assumptions on crystal habit mixture.

Existing parameterizations were typically built upon pre-assumed particle size distribution (PSDs) of droplets and crystals at desired LW or SW bands for particles within specific size ranges. There are several limitations when using pre-computed parameterizations in a GCM. Firstly, if the parameterized radiation bands for clouds do not match with that of the gas, a thick-averaging technique (Edwards & Slingo, 1996) is required to convert between two bands, introducing uncertainties and unnecessary computations.

Secondly, many existing schemes are only applicable to a limited size range (i.e., 4.2 to 16.6 µm of Slingo (1989)). As a result, radiation effects due to varying effective radii that are outside of the size limits cannot be simulated, limiting the full representation of the Twomey effect. While parameterizations exist for larger droplets and ice crystals to simulate the effects of precipitation, there is generally a lack of consistency between size and spectral ranges, when independently-developed parameterizations are used in GCMs.

Thirdly, existing optics parameterizations are typically built as a function of effective radii, which requires assumptions about PSD and crystal habit (single habit or mixture). However, these assumptions are not always consistent with the microphysics schemes in use. Variations in size and habit distributions have been shown to cause important radiation sensitivities (A. J. Baran, Hill, et al., 2014; Sieron et al., 2017; H. Yang et al., 2012; Zhang et al., 1999). Alternatively, studies have based ice optics parameterizations on ice water content (A. J. Baran, Hill, et al., 2014), aspect ratio (Fu, 2007), or a combination of crystal geometric properties (van Diedenhoven et al., 2014). While it is ideal to develop an optics parameterization using consistent assumptions on PSD, habit distribution, and size-mass relationship with the microphysics scheme used by the same GCM (e.g., A. J. Baran et al., 2016), such a simple and self-consistent approach is not always easy to implement. Adopting a more generalized approach, such as Slingo (1989) and Fu and Liou (1993), may likely induce biases caused by the inconsistent microphysics assumption, while adopting a flexible parameterization with multiple inputs may require a complex interface which poses challenges for climate model development. Although radiative sensitivity to size and habit distributions is well recognized, it remains unclear to what extent climate models can capture their impact on radiative energy using a simple and general method.

This study introduces a new tool for generating optics schemes for liquid droplets and ice crystals with varying PSDs and habits. The tool is implemented within the GFDL atmospheric model AM4-MG2 (Guo et al., 2021), with a focus on the longwave and shortwave spectral regions, which dominate radiative energy of Earth. Designed for compatibility with different radiation and microphysics schemes in GCMs, this tool provides flexibility in application. In Section 2, we provide an overview of the workflow, describe the method for generating a spectrally-resolved look-up-table, and then parameterize the optical properties as a rational function of effective radius at user-specified radiation bands. Section 3 describes the GCM implementation of the optics parameterization and an offline radiation package for evaluating the direct effects on CRE. In Section 4, we present the optical properties of liquid droplets and discuss the effects of PSD. In Section 5, the optical properties of ice particles are presented and the effects of crystal habits are discussed. Section 6 summarizes the result and discusses potential causes of uncertainties in the GCM when implementing the proposed scheme.
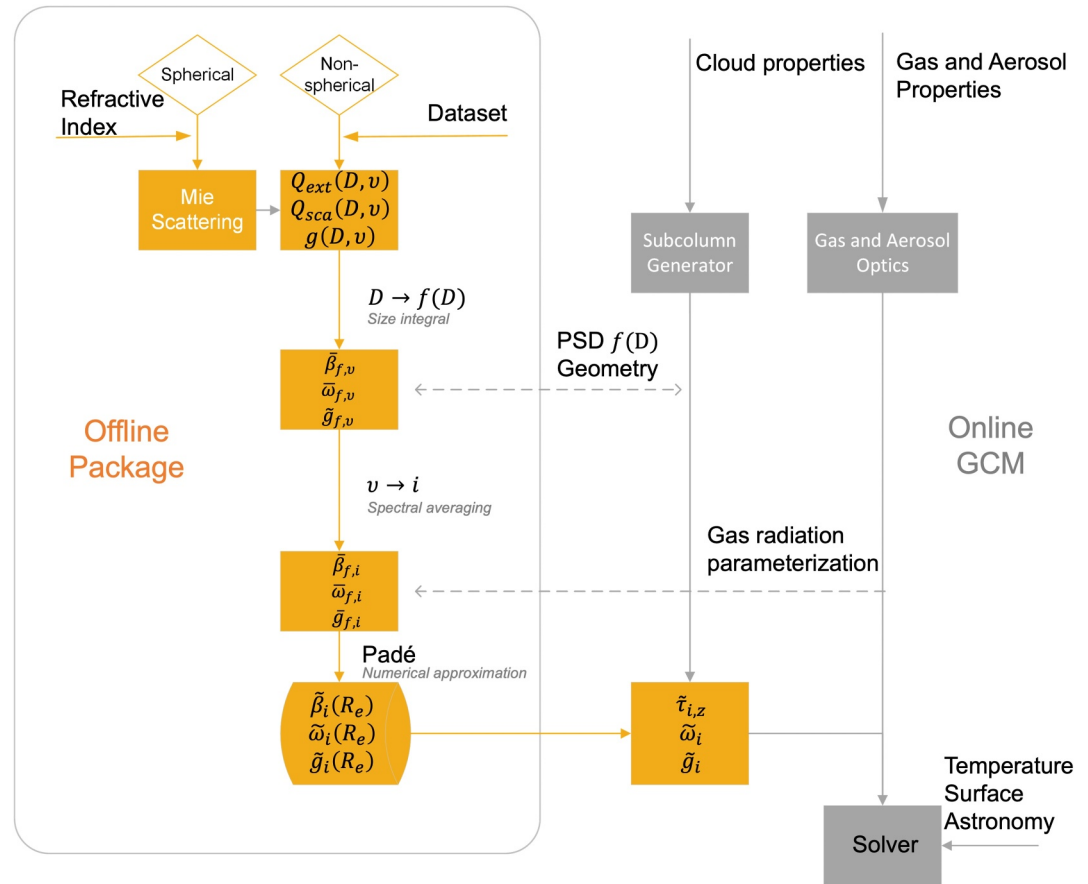
**Figure 1.** A schematic illustration of the workflow (orange), which interacts with other components of the radiation scheme in the general circulation model (gray). Here $D$ refers to the particle dimension of spherical particles or the maximum particle dimension of non-spherical particles, $R_e$ refers to the effective radius that represents an integral over particle size distribution ($f(D)$). $v$ refers to spectral wavenumber, and $i$ signifies an individual radiation band. Details are described in Section 2.

## 2. Overview and Method

This workflow consists of two components. As demonstrated in Figure 1, the first component is an offline package (shown in orange) that is used for generating optical properties at given radiation bands ($i$) over given PSDs and approximating the optical properties as a function of effective radius ($R_e$) The second component is an online calculation of optical properties (shown in gray). It takes in in-cloud water condensate mass, combines the micro-physical properties such as PSD and crystal geometry to obtain effective radius, and utilizes the parameterization to infer layer-by-layer optical depth ($\tilde{\tau}_{i,z}$), single-scattering albedo (SSA) ($\tilde{\omega}_{i,z}$), and asymmetry factor ($\tilde{g}_{i,z}$) by integrating water condensate over each model layer ($z$).

In the first step of the offline package, non-dimensional optical properties for single particles at various ranges of diameter $D$ are computed for every monochromatic spectral frequency ($v$) for extinction efficiency, $Q_{ext}(D,v)$, scattering efficiency, $Q_{sca}(D,v)$, and asymmetry factor, $g(D,v)$. The offline package uses well-established mie-scattering codes for spherical particles (i.e., droplets) and incorporates the data set by P. Yang et al. (2013) for non-spherical particles, such as various ice crystal habits. The package is also designed to accommodate other data sets, provided that their single-scattering properties are available in a similar format as P. Yang et al. (2013). Next, the optical properties for single particles at a range of spectral frequencies are integrated over a user-prescribed PSD, followed by an average over spectral frequency bounded by spectral bands used in the gas optics parameterization. These processes produce a two-dimensional look-up-table for extinction coefficient per condensate mass content (unit: $m^2g^{-1}$), SSA (non-dimensional), and asymmetry factor (non-dimensional) for every spectral band $i$. Finally, a Padé approximant is used to provide a rational

function of $R_e$ as $\tilde{\beta}_i(R_e)$ (unit: $m^2g^{-1}$), $\tilde{\omega}_i(R_e)$ (non-dimensional), and $\tilde{g}_i(R_e)$ (non-dimensional). These steps are demonstrated in Figure 1 and further described in this section. More specific descriptions and results for liquid and ice are presented in Sections 4 and 5.

### 2.1. Converting From Single Particle to Mean Over a Given PSD

A PSD, denoted as $f(D)$, describes the probability of particles occurring with diameter $D$. For ice, $D$ denotes the particle maximum dimension (Baum et al., 2005, 2011; Heymsfield et al., 2002, 2013). Here we consider a Gamma distribution for the size distribution, to be consistent with this two-moment stratiform cloud microphysics scheme (Guo et al., 2021; Morrison & Gettelman, 2008):

$$f(D) = N \frac{\lambda^a}{\Gamma(a)} D^{a-1} e^{-\lambda D} \tag{1}$$

Where $\Gamma$ is the Euler gamma function, $a$ is the shape parameter ($a = \mu - 1$ in Equation 1 of Morrison and Gettelman (2008)), $\lambda$ is the slope parameter, and $N$ is the number concentration. The Gamma distribution function is flexible and is able to describe the variation of PSD from exponential distribution ($a = 1$) to normal distribution (large $a$).

For an individual particle, its volume and projected area are denoted as $V(D)$ ($\mu m^3$) and $A(D)$ ($\mu m^2$), respectively. To be consistent with existing studies (Baum et al., 2011; P. Yang et al., 2013) and to avoid complexity caused by crystal habit, $V$ of ice particles refers to particle volume when being compressed into a compact sphere with a bulk density of ice at 917 $kgm^{-3}$, rather than their actual volume.

Optical properties over the PSD can be obtained by integrating over $f(D)$ as:

$$\bar{\beta}_{f,v} = \frac{\int_{D_{\min}}^{D_{\max}} Q_{ext}(D,v)A(D)f(D)dD}{\rho \int_{D_{\min}}^{D_{\max}} f(D)V(D)dD} \tag{2}$$

$$\bar{\omega}_{f,v} = \frac{\int_{D_{\min}}^{D_{\max}} Q_{sca}(D,v)A(D)f(D)dD}{\int_{D_{\min}}^{D_{\max}} Q_{ext}(D,v)A(D)f(D)dD} \tag{3}$$

$$\bar{g}_{f,v} = \frac{\int_{D_{\min}}^{D_{\max}} g(D,v)Q_{sca}(D,v)A(D)f(D)dD}{\int_{D_{\min}}^{D_{\max}} Q_{sca}(D,v)A(D)f(D)dD} \tag{4}$$

where $D_{\min}$ and $D_{\max}$ are the minimum and maximum diameter of the distribution, respectively. $\rho$ is the density of water at 997 $kgm^{-3}$ for liquid droplets, and bulk density of ice at 917 $kgm^{-3}$ for ice particles (Baum et al., 2011).

With user-specified PSD and particle volume-area-size relationship (as determined by crystal habit mixture), the mass extinction coefficient, SSA, and asymmetry factor are computed, providing a high-resolution look-up-table at each spectral wavenumber and an associated PSD. This high-resolution look-up-table is denoted as "hres" in Figures A1 and A3. Here the subscripts $f$ and $i$ denote the size and spectral wavenumber dimensions, respectively. It is used as a ground truth for building up the parameterization generated later in this study.

### 2.2. Converting From Single Spectral Frequency to Mean Over a Given Spectral Band

Gas optical properties in GCMs are typically parameterized within discrete spectral broadbands at selected spectral points based on the correlated-k method (Goody et al., 1989). In order to combine the optical properties of the gas and clouds, it is often assumed that the cloud optical properties are uniform within each spectral band. Therefore, it is necessary to convert optical properties calculated in Section 2.1 for spectral frequencies ($v$) to discrete spectral bands ($i$).

For each LW band, extinction coefficient, SSA, and asymmetry factor are converted from discrete wavenumbers to band following a "thin averaging" technique (Edwards & Slingo, 1996; Slingo & Schrecker, 1982):

$$\bar{\beta}_{f,i} = \frac{\int \bar{\beta}_{f,v} S(v) dv}{\int S(v) dv}$$

$$\bar{\omega}_{f,i} = \frac{\int \bar{\beta}_{f,v} \bar{\omega}_{f,v} S(v) dv}{\int \bar{\beta}_{f,v} S(v) dv}$$

$$\bar{g}_{f,i} = \frac{\int \bar{\beta}_{f,v} \bar{\omega}_{f,v} \bar{g}_{f,v} S(v) dv}{\int \bar{\beta}_{f,v} \bar{\omega}_{f,v} S(v) dv}$$

where $S(v)$ is the reference source function at every wavenumber; here we use the Planck function at 233 K for ice clouds and 250 K for liquid clouds.

For each SW band, the extinction coefficient and asymmetry factor are converted to bands following the formulas using the solar spectrum as the reference source function. For SSA, a "thick averaging" technique is required to properly represent the reflection of optically thick clouds (Edwards & Slingo, 1996). Following Equations 17 to 19 of Edwards and Slingo (1996), the SSA is converted as:

$$R_{\infty,v} = \frac{1 - \sqrt{\dfrac{1 - \bar{\omega}_{f,v} \bar{g}_{f,v}}{1 - \bar{\omega}_{f,v}}}}{1 + \sqrt{\dfrac{1 - \bar{\omega}_{f,v} \bar{g}_{f,v}}{1 - \bar{\omega}_{f,v}}}}$$

$$R_{\infty,i} = \frac{\int \bar{R}_{\infty,v} S(v) dv}{\int S(v) dv}$$

$$\bar{\omega}_{f,i} = \frac{4 R_{\infty,i}}{(1 + R_{\infty,i})^2 - \bar{g}_{f,i} (1 - R_{\infty,i})^2}$$

where $R_{\infty,v}$ and $R_{\infty,i}$ is the reflection of thick clouds at wavenumber $v$ and band $i$, respectively.

Here we adopt the gas optics developed in RRTMGP (Pincus et al., 2019) as an example. It contains 16 bands in LW from 10 to 3,250 cm$^{-1}$ and 14 bands in SW from 820 to 50,000 cm$^{-1}$. $\bar{\beta}_{f,i}$, $\bar{\omega}_{f,i}$, and $\bar{g}_{f,i}$ at every spectral band are used to build up another look-up-table (denoted as "band" in figures presented in Sections 4 and 5, and the appendices) to validate the parameterizations.

## 2.3. Generating Padé Approximate

Sections 2.1 and 2.2 provide look-up-tables of optical properties at spectral wavenumbers or bands for given hydrometeors with the prescribed PSD. While various combinations of microphysical properties can be assumed when generating these look-up tables, only a subset of these variations are resolved by GCM and are required to capture the optical effects. The effective radius, $R_e$, has been introduced and is widely used to represent the bulk average over a given PSD. It is defined as:

$$R_e = \frac{3}{4} \frac{\int_{D_{\min}}^{D_{\max}} f(D) V(D) dD}{\int_{D_{\min}}^{D_{\max}} f(D) A(D) dD} \tag{5}$$

where $R_e$ quantifies the mean volume-to-area ratio (A. Baran & Francis, 2004; Baum et al., 2005; Hansen & Pollack, 1970; Hu & Stamnes, 1993; McFarquhar & Heymsfield, 1998; Morrison & Gettelman, 2008; Slingo, 1989). In the following context of this paper, we use $R_e$ to construct numerical parameterizations, validate their accuracy and numerical stability by comparing with look-up-tables generated with the same set of microphysics assumptions, and evaluate uncertainties arising from variations in microphysics by comparing with look-up tables generated using different assumptions that yield the same $R_e$.

The look-up table generated from Section 2.2 can be directly used in radiative transfer codes via performing a round-up or linear interpolation over the discrete data. However, this process may not be numerically accurate.

Here we adopt a Padé approximate (Baker & Gammel, 1961) to describe the optical properties as a continuous, rational function of $R_e$, so that no extra interpolation is performed when being implemented. It is a numerically stable approach that provides a high-order approximation of a function and reduces biases in existing parameterizations as found in Hogan and Bozzo (2018). Padé approximate is used here as a general fitting formulation $\left(\tilde{F}(R_e)\right)$ as a function of $R_e$ for $\tilde{\beta}_i(R_e)$, $\tilde{\omega}_i(R_e)$, $\tilde{g}_i(R_e)$ at every band $i$:

$$\tilde{F}(R_e) = \frac{p_2 + p_1 R_e + p_0 R_e^2}{q_2 + q_1 R_e + q_0 R_e^2} \tag{6}$$

In this function, $q_0$, $q_1$, and $q_2$ are real, positive numbers to ensure that the denominator is always positive for a numerically stable approximation within the prescribed size range. In case of over-fitting, $p_0$, $q_1$, and $q_0$ are set to be zero which is equivalent to a piece-wise linear fit. Optical properties inferred from parameterized Equation 6 are denoted as "pade" hereinafter.

## 3. Implementation and Evaluation Methods

### 3.1. Implementations in GCM

With given in-cloud effective radius $R_e$, the layer-by-layer mass extinction coefficient, SSA and asymmetry factor can be then obtained from the parameterization as $\tilde{\beta}_i(R_e)$, $\tilde{\omega}_i(R_e)$ and $\tilde{g}_i(R_e)$, respectively, for every type of water condensate, using Equation 6 and the Padé coefficients. The parameterized extinction coefficients $\tilde{\beta}_i(R_e)$ are converted to layer-by-layer optical depths $(\tilde{\tau}_{i,z})$ using in-cloud condensate $q_c$, effective radius $(R_e)$, and layer thickness $(dz)$ as:

$$\tilde{\tau}_{i,z} = \tilde{\beta}_i(R_e) q_c dz \tag{7}$$

The optical depth, SSA, and asymmetry factor jointly determine the CRE when cloud and atmospheric conditions are specified. Figure 2 presents the effects of these properties on cloud reflection, transmittance, and absorptance, based on a two-stream solution derived from Petty (2023). The reflection, transmittance, and absorptance can be further linked with the CRE presented in Sections 4 and 5. In Figure 2, a "+" sign refers to changes in fluxes that lead to an increase in atmospheric absorption; more specifically, an increase in net downwelling radiation at the TOA or an increase in net upwelling radiation at the surface. The figure indicates that clouds tend to be more reflective (red in upper rows of Figure 2) with higher optical depth, higher SSA, and lower asymmetry factor, thereby enhancing the upwelling SW fluxes at the TOA ("−"). Clouds are more transparent (red in mid rows of Figure 2) to LW and SW fluxes with lower optical depth, higher SSA, and higher asymmetry factor, increasing upwelling LW fluxes at the TOA ("−") and downwelling SW fluxes at the surface ("−"). Cloud absorption tends to increase with higher optical depth, lower SSA, and higher asymmetry factor, leading to increased cloud absorption of SW radiation. The effects on LW ATM absorption is sensitive to temperature and vertical distribution of the cloud, thus cannot be determined by these changes in optical properties.

When implemented in GCMs, these optical properties are inferred from particle size, for which the effective radius is often used. The dependence on $R_e$ is necessary because it critically controls the optical depth and asymmetry factor. If $Q_{ext}$ is insensitive to particle size, Equation 7 yields:

$$\tilde{\tau}_{i,z} \propto \frac{q_c dz}{R_e} \tag{8}$$

As a result, the optical depth is controlled by condensate mass concentration and effective radius via $q_c/R_e$ to first order and is less sensitive to PSD and crystal habit of clouds. Although Equation 8 only holds strictly in the geometric optics regime (when $Q_{ext} \approx 2$), the strong relationship between $R_e$ and optical depth supports the choice of using $R_e$ to represent optical depth of clouds when building up the optic schemes in Section 2.

Despite the dominant control of effective radii on optical depth, the effective radii are not always resolved by microphysics schemes in GCMs, because the PSD and crystal habit are sometimes prescribed, even when water
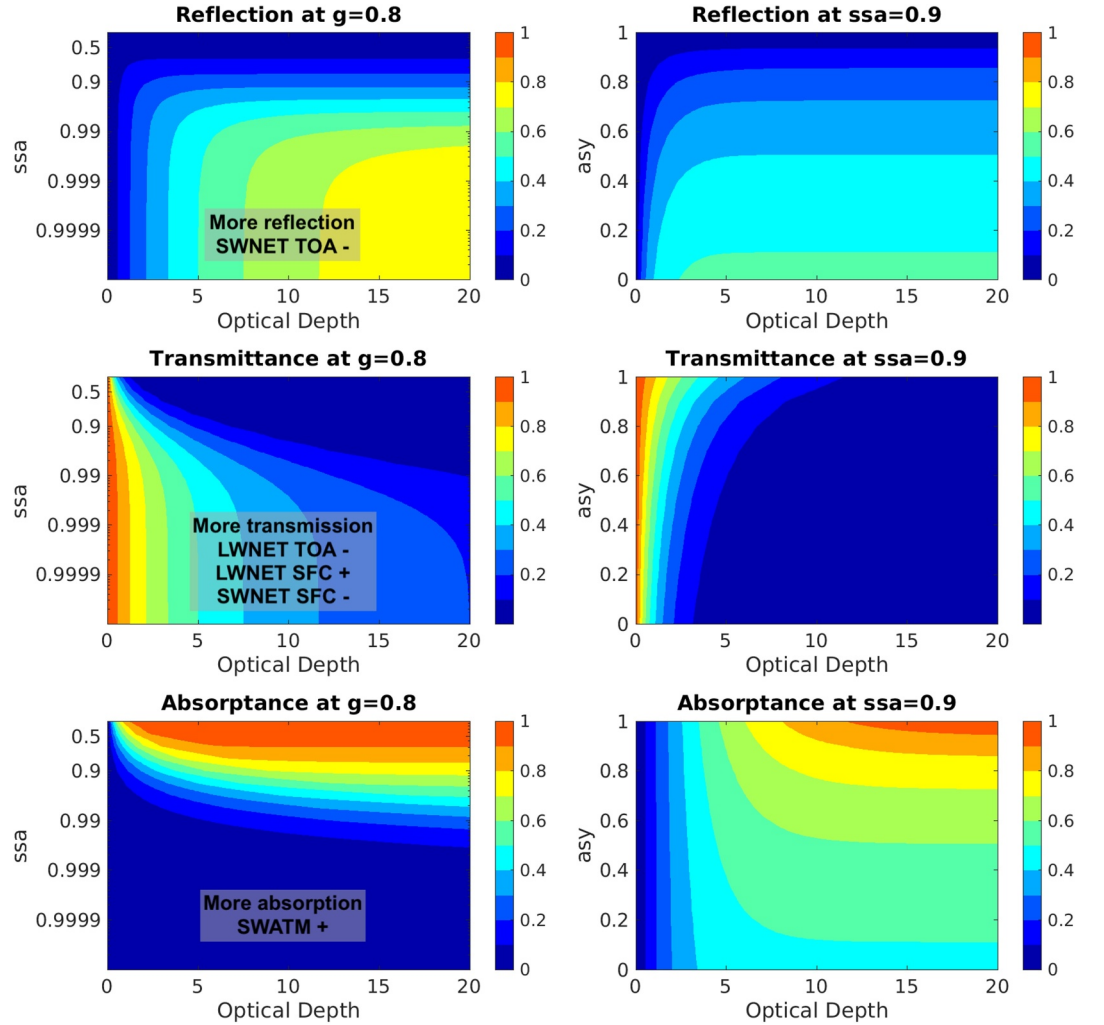
**Figure 2.** Sensitivity in cloud reflection (Equation 13.65 in Petty (2023)), transmittance (Equation 13.66 in Petty (2023)), and absorptance to optical depth (OD), single-scattering albedo, and asymmetry factor (ASY). Annotations on the right summarize the effects of these optical properties on the CRE. " +" means perturbations in these properties lead to enhanced atmospheric absorption by clouds or precipitation (downward positive at the top of the atmosphere).

content (CWC) and number concentration (N) are predicted. With any two-moment microphysics scheme that predicts CWC and N, a mean radius of an equivalent solid sphere $R_v$ can be computed as:

$$R_v = \left(\frac{3q_c}{4\pi\rho N}\right)^{\frac{1}{3}} \tag{9}$$

One may define a ratio between $R_v$ to $R_e$ as:

$$r = \frac{R_e}{R_v} \tag{10}$$

This $r$ is referred to as the volume-to-radius ratio, similar to Lohmann and Roeckner (1996). If PSD (e.g., $a$ in Equation 1) and crystal habit are fixed at a prescribed condition, this $r$ is a constant. As a result, models that fix PSD and habit at a prescribed condition determine optical depth using Equation 8 by $q_c$ and $N$. The optical depth of these models can be biased because they neglect the extra degrees of freedom from varying PSD and habit; to overcome potential biases, a parameterization that varies $r$ is required for representing effects from PSD and habit on $R_e$ and is further discussed in Sections 4 and 5.

**Table 1**
*A Summary of Cloud and Optics Parameterizations Generated in This Study and Existing Parameterizations Used in AM4-MG2 (Guo et al., 2021)*

| | Optics in AM4-MG2 | | | | New optics | | |
|---|---|---|---|---|---|---|---|
| | Ref | $R_e$ range | PSD | Habit | $R_e$ range | Gamma PSD | Habit |
| Liquid cloud | LW: Held et al. (1993) | 4.2 to 16.6 μm | – | – | 0.25 to 17,300 μm | Equation 1 | – |
| | SW: Slingo (1989) | | Gamma | | | $a = 12$ | |
| Rain | LW: Fu et al. (1995) | 16.6 to 2000 μm | Truncated constant-slope Gamma log-normal | – | | | |
| | SW: Savijärvi (1997) | | | | | | |
| Ice Cloud | LW: Fu and Liou (1993) | 9.3 to 65.1 μm | Heymsfield and Platt (1984) | Spheroid and hexagonal | 2.5 to 5,000 μm | Equation 1 | Severely roughened solid column |
| | SW: Fu (1996) | | | | | $a = 1$ | $r$ in Equation 15 for clouds |
| Snow | Fu et al. (1995) | 60 to 1,800 μm | Truncated constant-slope Gamma | Sphere | | | $r = 0.5$ for snow |

### 3.2. Evaluations in an Offline Model

In the following section of this paper, we evaluate the direct effects of optics schemes on the CRE using a standalone version of the radiation code used by GFDL's AM4-MG2 (Guo et al., 2021) as an example. AM4-MG2 is based on GFDL's Atmosphere Model version 4.0 (AM4.0) (Zhao et al., 2018a, 2018b). The major differences between AM4-MG2 and AM4.0 lie in their cloud microphysics (Gettelman & Morrison, 2015) and ice nucleation parameterizations (Fan et al., 2019). As described in Figure 1, microphysics schemes in the GCM generate grid-cell-mean cloud properties, including cloud fraction, condensate water content for cloud liquid, cloud ice, rain, and snow, as well as number concentration and mean size of each type of condensate. In AM4-MG2, these grid-cell-mean cloud properties are converted to in-cloud properties for each stochastically generated subcolumn following Pincus et al. (2006), providing in-cloud condensate $q_c$, in-cloud effective radius, $R_e$, and in-cloud number concentration $N$. The standalone version of the radiation code uses RTE-RRTMGP (Pincus et al., 2019) for the gas optics and radiative solver. It adopts a rescaling approximation to account for LW scattering effects (Tang et al., 2018). It takes in 3-hourly surface and atmospheric conditions generated from other components of the model for 1 year. This offline computation does not affect the actual model run. In the following context of this paper, we implement different optics parameterizations in the same offline code with identical inputs. The direct effects of optics parameterizations are then computed as differences in annual mean radiation fluxes obtained from these experiments.

AM4-MG2 utilizes a list of optics schemes to parameterize the optical properties of liquid clouds, ice clouds, rain, and snow in the LW and SW spectrum separately, as summarized in Table 1. These existing parameterizations are converted to the radiation bands of RTE-RRTMGP using the same thick-average technique (Edwards & Slingo, 1996). They are shown in the right panels of Figures 4 and 6 and are further compared to the new scheme in Sections 4 and 5.

### 3.3. Comparisons With Satellite Observations

We use the Clouds and the Earth's Radiant Energy System (CERES) Energy Balanced and Filled (EBAF) v4.2 product (Kato et al., 2018; Loeb et al., 2018) as an observational reference to evaluate potential biases in the modeled cloud radiative effect (CRE). CERES instruments measure radiances in the shortwave, window, and total wavelength bands. These measurements are combined with data from the Moderate Resolution Imaging Spectroradiometer (MODIS) to produce long-term, globally gridded estimates of radiative fluxes at TOA and at the surface. The CRE of the EBAF product are derived from the CERES cloud algorithm (Minnis et al., 2020; Trepte et al., 2019), which uses the optical properties of roughened hexagonal ice columns (P. Yang et al., 2008).

We conduct an AMIP simulation using AM4-MG2 and compare it with CERES EBAF observations for the average period over 2003 to 2020. As described in Section 3.2, AM4-MG2 uses the GFDL radiation code and

**Table 2**
*Global-Mean, Annual-Mean Cloud Effects [Wm$^{-2}$] Due To Changes in Cloud and Precipitation Optics Parameterizations on Radiation Fluxes at Top-of-Atmosphere (the Top of the Atmosphere), Surface (SFC), and Atmospheric Absorption (ATM), in Longwave (LW), Shortwave (SW), and the Sum of Two Broadbands (Net) Respectively*

|  |  | LW TOA | LW ATM | SW TOA | SW ATM | Net ATM |
|---|---|---|---|---|---|---|
| Climatological CRE |  | + | − | − | + | +/− |
| Biases in CRE CERES minus GFDL AM4-MG2, 2000 to 2020 |  | 3.76 | −2.43 | 2.47 | −0.50 | −2.93 |
| Optics Scheme | Total Optics | 0.24 | 0.09 | −1.08 | −1.21 | −1.12 |
|  | Liq Clouds | 0.10 | 0.44 | 1.50 | −0.14 | 0.30 |
|  | Rain | 0.10 | −0.27 | −0.13 | −0.13 | −0.40 |
|  | Ice Clouds | −0.05 | −0.12 | −1.62 | −0.88 | −1.00 |
|  | Snow | 0.08 | 0.06 | −0.26 | −0.04 | 0.02 |
| Liq $R_e$ Range |  | 0.01 | −0.02 | −0.57 | 0.02 | −0.03 |
| Nonspherical Ice $R_e$ |  | 3.20 | 2.58 | −2.76 | −0.55 | 2.03 |
| Maximum Estimates of Potential Biases | PSD ($a = 1$ vs. $a = 12$) | −0.04 | 0.01 | −0.48 | −0.03 | −0.02 |
|  | Habit (Plate10ele vs. Solid column) | −0.82 | −0.75 | 1.37 | 0.30 | −0.44 |

*Note.* A positive sign means changes in the CRE enhance atmospheric absorption (downward positive at the TOA), consistent with Figure 2.

existing cloud optic parameterizations, including Held et al. (1993), Slingo (1989), Fu and Liou (1993), Fu (1996), and Savijärvi (1997), as summarized in Table 1.

Table 2 and the gray curves in Figure 3 (labeled "CERES-AM4cld") show differences between the modeled and observed CRE. When the sign of these differences matches the sign of the climatological CRE in Table 2, it indicates that AM4-MG2 simulates a weaker CRE than inferred from CERES EBAF. Overall, the model produces weaker global mean LW CRE and stronger CRE SW, largely consistent with AM4 (Zhao et al., 2018a). Zhao et al. (2018b) suggests that these relatively small global-mean biases in CRE are achieved by tuning of parameters related to cloud processes, with the remaining biases caused by compensating effects from excessive thick clouds and insufficient low-level cloud cover. A more recent study by Guo et al. (2024) has shown that AM4-MG2 produces similar biases in cloud properties, with detailed comparison using the COSP satellite simulator (Bodas-Salcedo et al., 2011).

Overall, the excessive thick clouds can lead to an overestimated SW TOA CRE by the model. The insufficient low-level cloud cover can reduce the atmospheric trapping effect, leading to weaker LW atmospheric CRE and weaker SW CRE not only in the tropics but also at high latitudes. However, it should be noted that there are large discrepancies in high latitude low-level clouds among satellite products (e.g., MODIS vs. active sensors) (Chan & Comiso, 2013; Guo et al., 2024; Yost et al., 2020) and relatively large uncertainties in CERES surface fluxes (over 10 Wm$^{-2}$ in polar regions (Kato et al., 2018)).

These comparisons with CERES EBAF serve as a baseline to understand whether updating the cloud optics scheme can improve agreement with satellite observations. In Sections 4 and 5, we evaluate our new parameterization in an offline radiation code and examine the resulting differences in CRE. Because the offline approach does not alter the simulated cloud fields, we do not expect existing biases caused by biases in cloud fraction or cloud water path to be overcome by cloud optics. If the differences caused by cloud optics overlap with the gray curves in Figure 3, it would imply that the existing model biases are explained by cloud optics, with the remaining differences caused by biases in the simulated cloud properties.

## 4. Parameterization of Liquid Cloud and Rain

Liquid clouds and rain are droplets with different size ranges and are usually treated as sphere particles in existing studies (Fu et al., 1995; Hu & Stamnes, 1993; Savijärvi, 1997; Savijärvi & Räisänen, 1998; Slingo & Schrecker, 1982), using the well-established Mie scattering theory (Mätzler, 2002; Mie, 1908). The Mie scattering theory describes the optical properties as a function of size parameter, which is defined as:
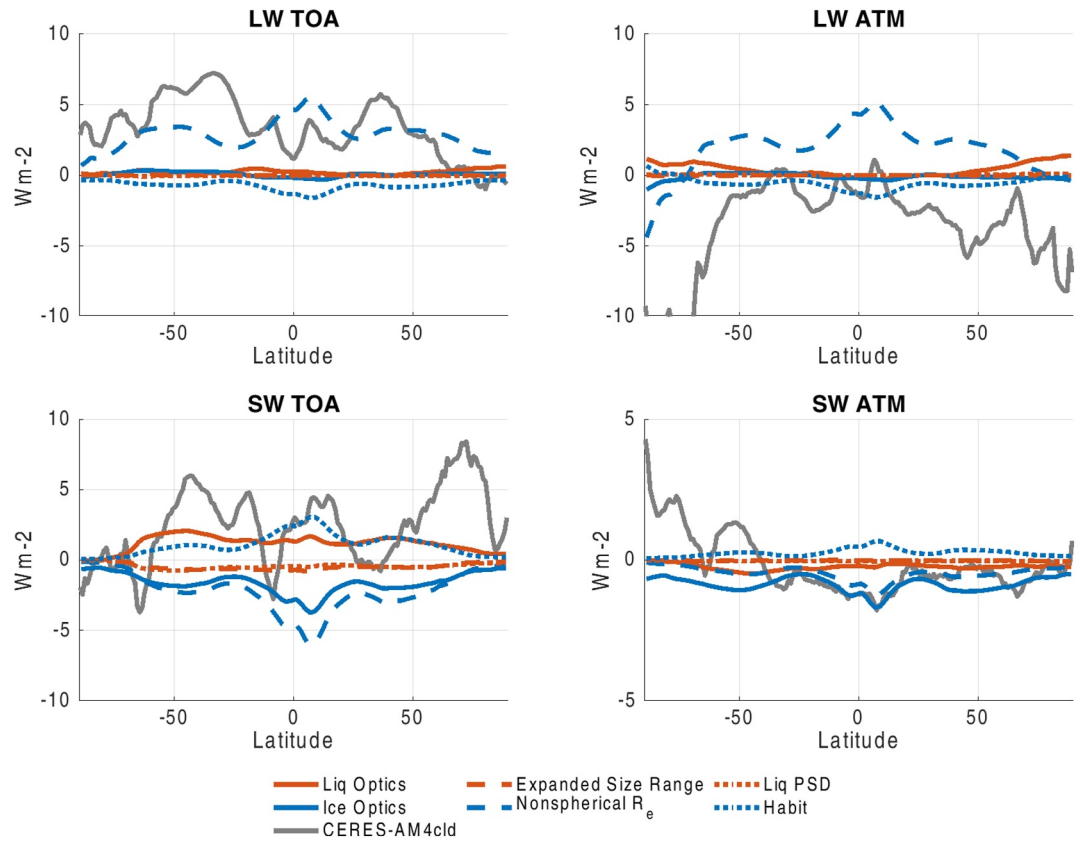
**Figure 3.** Zonal-mean, annual-mean cloud effects due to changes in cloud and precipitation optics parameterizations on net downwelling fluxes at top-of-atmosphere (the top of the atmosphere) and net atmospheric absorption (ATM), in longwave (LW) and shortwave (SW) respectively. Global-mean effects are summarized in Table 2. Annual-mean global pattern of the CRE changes are presented in Figures A5–A9 and 8. Gray curves are biases in CRE of AMIP simulation compared to CERES Energy Balanced and Filled v4.2 for the period of 2000–2020.

$$x = \pi D \upsilon \qquad (11)$$

This non-dimensional size parameter evaluates the relationship between the size of the particles and the incident wavelength ($1/\upsilon$). When $x$ is much larger than 1, geometric scattering occurs. Because the Mie scattering theory converges to the limit of geometric optics for large particles ($Q_{ext} = 2$), it is also applicable to rain droplets. Therefore, performing a Mie-scattering calculation for a wide range of individual particles (i.e., 0.1 to 15,000 μm) and then following the procedure described in Sections 2.1, 2.2, and 2.3, is sufficient to describe the optical properties of liquid clouds and rain at the same time. In this process, refractive indices from $10^{-3}$ to $10^{6}$ cm$^{-1}$ wavenumber are used, based on Segelstein (1981). Six size ranges are used to minimize the biases caused by the numerical approximation: 0.1 to 1, 1 to 10, 10 to 50, 50 to 100, 100 to 1,000, and 1,000 to 17,300 μm.

Adopting $a = 12$ in the Gamma distribution (Equation 1), optical properties at the native resolution of the refractive indices are generated following Section 2.1. These optical properties are shown in Figure A1 as a function of band-center wavenumbers. In Figures A2 and 4, the optical properties are also displayed as a function of $R_e$ since a PSD ($f(D)$) is mapped with a unique $R_e$ when the shape parameter is fixed. Band-by-band optical properties generated from Section 2.2 are shown in the left column of Figure 4 and the properties inferred from the Padé approximate ($\tilde{\beta}_i(R_e)$, $\tilde{\omega}_i(R_e)$, and $\tilde{g}_i(R_e)$) are shown in the right column. More detailed comparisons conducted in Figures A1 and A2 confirm that biases resulting from the Padé approximate are small across wide size ranges for all wavenumbers and bands.

In general, smaller droplets exhibit stronger spectral dependence than larger droplets, which are more uniform across the spectrum, especially as they approach the geometric scattering limit. Liquid droplets are more
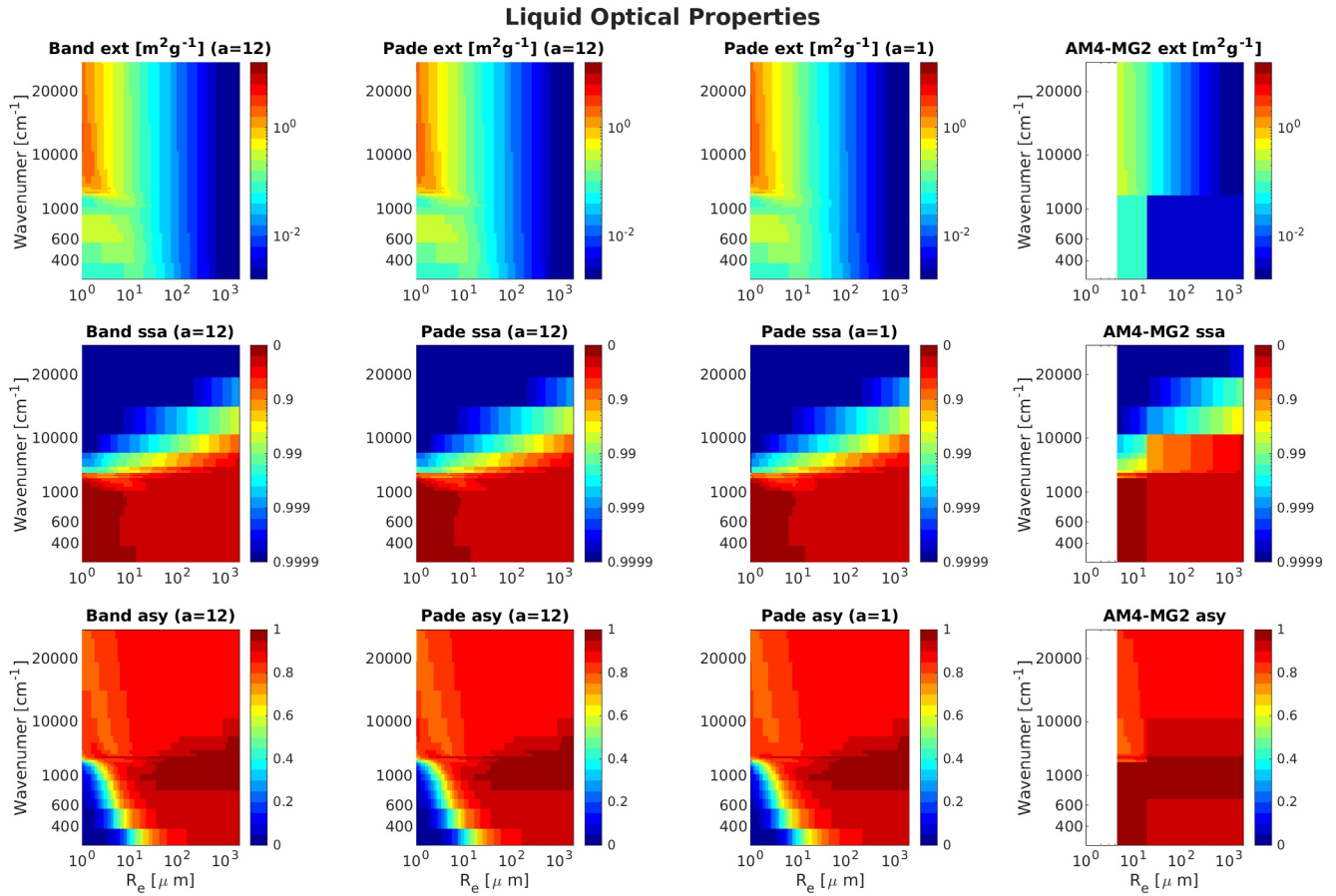
## Liquid Optical Properties



**Figure 4.** Optical properties of droplets as a function of wavenumber [cm$^{-1}$] for effective radius ($R_e$), assuming the shape parameter of particle size distribution ($a$) equals to 12. Top: mass extinction coefficient [m$^2$g$^{-1}$]. Middle: single-scattering albedo. Bottom: asymmetry factor. The first column shows band-by-band optical properties generated from Equations 2–4. The second column shows optical properties inferred from the Padé Approximate following Equation 6. The third column shows the same as the second column but for $a$ at 1. The right column shows optical properties inferred from existing parameterizations used in AM4-MG2 (Guo et al., 2021), based on Held et al. (1993) and Slingo (1989) for LW and SW liquid clouds (4.2–16.6 µm), Fu et al. (1995) and Savijärvi (1997) for LW and SW raindrops (16.6–5,000 µm), respectively. Detailed comparisons at specific bands and effective radii are presented in Figures A1 and A2.

absorptive in the LW (i.e., below 3,250 cm$^{-1}$) and more reflective in SW, as indicated by the middle panels in Figure 4. Figure 4 also shows the strong size dependency of the optical properties. In the LW, the mass extinction coefficient is relatively constant at 0.25 m$^2$g$^{-1}$ (Figure A2a) when $R_e$ is small and then decays with $R_e$, as expected from Equation 8. The SSA increases with $R_e$ until reaching a relatively constant value at 0.45, while the asymmetry factor increases with $R_e$ until reaching 0.92. In SW, mass extinction coefficient and SSA tend to decrease with $R_e$ and the asymmetry factor is relatively constant (bottom panels in Figure A2).

### 4.1. Effects of Particle Size Distribution

This section aims to investigate the impacts of varying PSDs on the optical properties of liquid droplets. In particular, here we aim to achieve consistency with Morrison and Gettelman (2008) and Guo et al. (2021), who deploy a varying shape parameter ($a$) in the Gamma PSD (Equation 1).

As shown in Equation 9, given in-cloud condensation mass and number concentration generated from microphysics schemes, one may infer a mean equivalent radius of a sphere, $R_v$, that is independent of PSD. Figure 5a then shows various PSDs generated from a wide range of gamma shape parameters ($a$) while conserving $R_v$ at 10 µm. The various PSDs result in distinct effective radii $R_e$. For spherical particles with a Gamma size distribution, $R_e$ and $R_v$ can be derived analytically as:
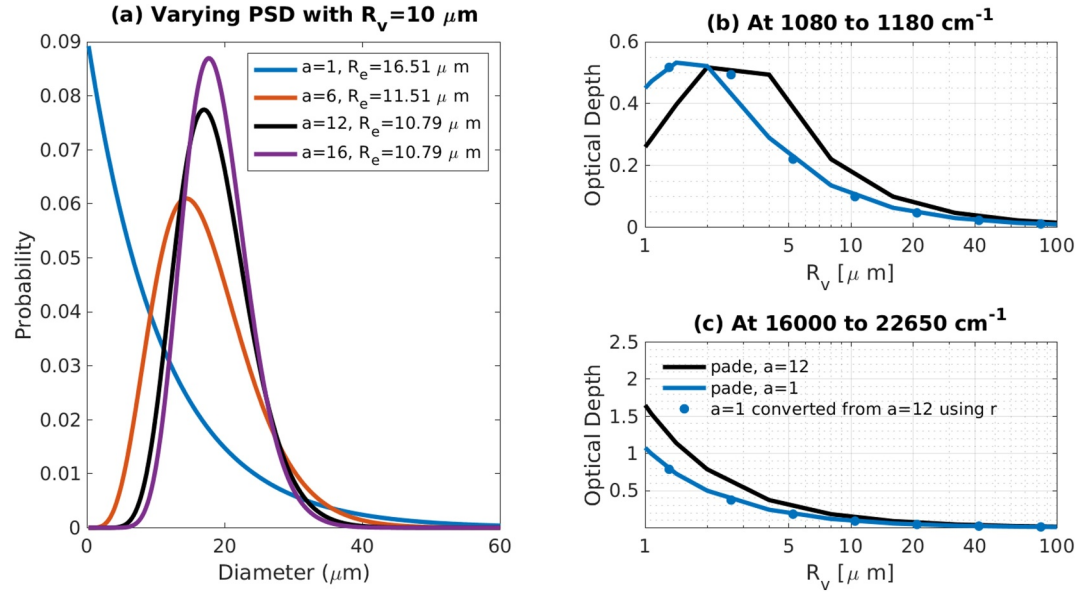
**Figure 5.** (a) Gamma probability function of single particle diameter (μm) with varying shape parameter ($a$) that yields $R_v$ at 10 μm. Optical depth liquid droplets (assuming 10 gm$^{-2}$ of condensate water path) at the same $R_v$ for $a = 12$ (black) and $a = 1$ (blue), in longwave (b) and shortwave (c). Solid lines are the actual optical depth at different $a$, and markers are optical depth inferred from $a = 12$ at the same $R_e$. A spectrally-resolved comparison similar to (b, c) is shown in Figure A1.

$$R_v = \frac{[a(a+1)(a+2)]^{1/3}}{\lambda} \tag{12}$$

$$R_e = \frac{a+2}{\lambda} \tag{13}$$

As explained in Equation 8, the mass extinction coefficient is roughly proportional to $1/R_e$, particularly for particles and wavenumbers that have large size parameters ($x$). Figures 5b and 5c shows the optical depth of liquid clouds (assuming 10 gm$^{-2}$ of cloud water path) as solid curves, using the mass extinction coefficients generated over two spectral ranges: 1,080–1,180 cm$^{-1}$ (infrared window) and 16,000–22,650 cm$^{-1}$ (the peak of solar spectrum). Figures 5b and 5c confirms that, given a fixed $R_v$ (the same number concentration), droplets become more opaque as $a$ increases, since larger $a$ yields smaller $R_e$. Assuming the optical depth at the same $R_e$ does not depend on $a$, one can infer the optical depth for $a = 1$ from that of $a = 12$ by converting $R_e$ to $R_v$, shown by the blue markers in Figures 5b and 5c). We choose $a = 1$ here because (a) it corresponds to the parameter used in PSD of raindrops in Gettelman and Morrison (2015) and (Guo et al., 2021) and (b) it represents the most dramatic change from $a = 12$ and has a stronger weight on the small size range (blue in Figure 5a, converges to the exponential distribution). The close match between the blue curves and markers in Figure 5 confirms that optical depth is largely a function of $R_e$ and is less sensitive to the PSD.

Figures 4, A2, and A1 provide a more detailed comparison of $a = 1$ and $a = 12$ for the mass extinction coefficients, SSA, and the asymmetry factor. The differences at the same $R_e$ are generally within 10%. The largest deviations appear in the longwave spectrum at small $R_e$ (where geometric scattering does not hold); this range is magnified in Figure 5b, confirming that the discrepancies remain much smaller than the $R_e$ dependency. Therefore, if radiative transfer codes and microphysics processes adopt a consistent definition in effective radius (following Equation 5), variations in PSDs are expected to have minor impacts on the cloud radiative effect.

For a microphysics scheme that cannot predict PSD, the volume-to-radius ratio, $r$, is necessary for inferring the effective radius $R_e$ from $R_v$. Using a Gamma size distribution with unknown shape parameter $a$ as an example, and combining Equations 11 and 12, $r$ can be expressed as:
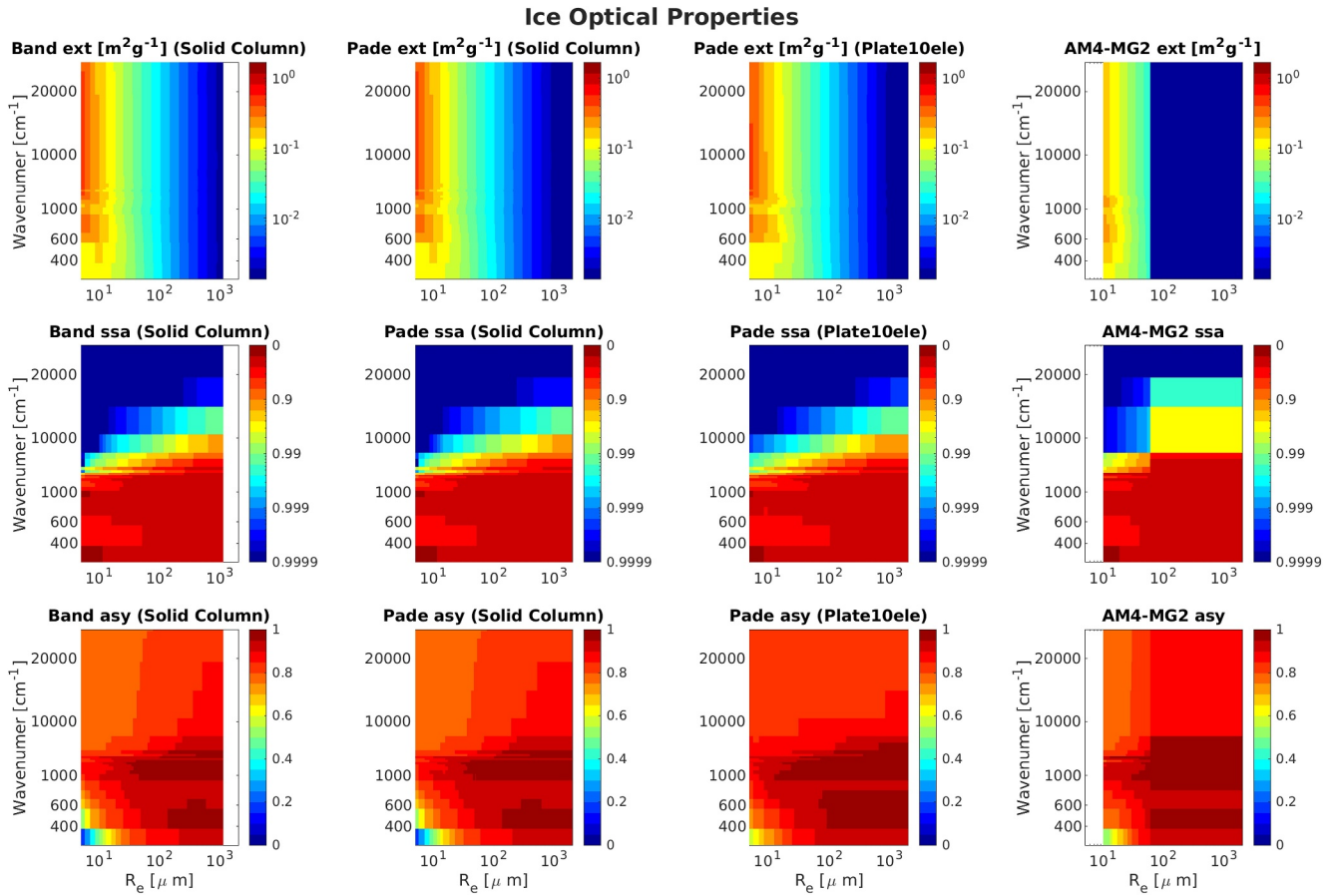
**Figure 6.** Similar to Figure 4, optical properties of severely roughened solid column as a function of wavenumber [cm$^{-1}$] for effective radius ($R_e$). The third column shows the optical properties of severely roughened and heavily aggregated plates. The right column shows optical properties inferred from existing parameterizations used in AM4-MG2 (Guo et al., 2021), based on Fu and Liou (1993) and Fu (1996) for longwave and shortwave ice clouds (9.3–65.1 μm), respectively. Fu et al. (1995) is used for ice precipitation (60–5,000 μm). Detailed comparisons at specific bands and effective radii are presented in Figures A1 and A2.

$$r = \frac{(a+2)^{\frac{2}{3}}}{[a(a+1)]^{\frac{1}{3}}}$$

(14)

where the lower limit of $r$ is 1. Typical $r$ values are estimated here for reference purposes. For rain droplets, $a$ is set to be 1 by Morrison and Gettelman (2008), resulting in $r = 1.651$. For cloud droplets, reference $r$ values have also been given in Lohmann and Roeckner (1996) based on Martin et al. (1994), with $r = 1.077$ for maritime clouds and $r = 1.143$ for continental clouds. The lower limit of $a$ at 3 is set by Morrison and Gettelman (2008) with abundant cloud condensation nuclei, following aircraft observations in stratocumulus cloud conducted by Martin et al. (1994), corresponding to an upper limit at $r = 1.28$ of liquid clouds. Although the exact formulations may vary, these prescribed $r$ values have been widely used to describe that effective radii are relatively larger than $R_v$ with abundant cloud condensation nuclei. For example, Martin et al. (1994) shows that with the same $R_v$, the effective radius of polluted continental clouds is larger than unpolluted clouds. The different conversions from $R_v$ to effective radius for continental and maritime clouds derived from Martin et al. (1994) are adopted by existing GCMs, such as Lohmann and Roeckner (1996) and Zhao et al. (2018a).

Because AM4-MG2 resolves the PSD effects on $R_e$, it is possible to adopt a single set of optics parameterizations using a prescribed shape parameter ($a$) for liquid droplets. We assume $a = 12$ for both liquid and rain to achieve a seamless transition from small to large droplets. $a = 12$ is used here because it is a typical value for liquid clouds in Guo et al. (2021) for reducing potential biases caused by varying PSD at small size (i.e., for which the Mie scattering rather than geometric scattering dominates). Using the new optics parameterization achieves

consistency in the optical properties between the LW and SW band and between the liquid clouds and rain, and greatly expands the applicable range of $R_e$ (0.25–17,300 μm).

### 4.2. Comparison With Existing Schemes

Here we utilize the offline radiation code described in Section 3 to compute the annual-mean radiation fluxes using existing liquid parameterizations (Fu et al., 1995; Held et al., 1993; Savijärvi, 1997; Slingo, 1989) and new parameterizations for $a = 12$. We evaluate the effects of this parameterization based on annual mean radiation fluxes at the top-of-atmosphere (TOA), surface, and atmosphere, in LW and SW bands separately. When presenting zonal-mean and global-mean effects in Figure 3 and Table 2, an increase in the magnitude of these quantities leads to enhanced atmospheric absorption.

Figures 4, A1, and A2 present the optical properties of liquid generated from existing parameterizations used in AM4-MG2. These parameterizations include Held et al. (1993) for LW liquid clouds, Slingo (1989) for SW ice clouds, Fu et al. (1995) for LW rain, and Savijärvi (1997) for SW rain. As visualized in Figure 4, existing parameterizations have some limitations. Firstly, Held et al. (1993) and Fu et al. (1995) have no size dependency, leading to large biases in the LW mass extinction coefficient. Secondly, the applicable $R_e$ range is limited to 4.2 to 16.6 μm for liquid clouds. This may limit the ability to simulate the well-known Twomey effect (Twomey, 1977), where liquid clouds become more reflective with decreasing $R_e$ when droplet concentration increases (i.e., bottom left panel of Figure A2). Lastly, substantial discrepancies are found across the size range of liquid and rain and across LW and SW bands (abrupt transitions in Figures 4, A1, and A2). It is noteworthy that these existing parameterizations were developed independently in the past to fulfill specific requirements of microphysics schemes, rather than as a consequence of disparities in the physical representation of liquid clouds and raindrops.

These limitations are overcome in the new liquid optics scheme generated in Section 3, using a Gamma shape parameter $a = 12$. By adopting the same liquid cloud effective radius range used in Slingo (1989) (4.2–16.6 μm), we evaluate the effects caused by replacing the existing parameterizations within the same size range. For LW liquid, Held et al. (1993) assumes a constant LW mass extinction coefficient for liquid clouds at 0.1 m$^2$g$^{-1}$, which is weaker than the actual mass extinction coefficient (top panels of Figures 4 and A2). As a result, it underestimates the LW cloud effects at the TOA. Because Held et al. (1993) neglects the LW scattering effects (i.e., $\omega = 0$), it overestimates the LW CRE at the surface. For SW liquid, Slingo (1989) tends to overestimate the mass extinction coefficient for $R_e$ larger than 10 μm, leading it to overestimate the TOA CRE by 1.5 Wm$^{-2}$ and the surface CRE by 1.64 Wm$^{-2}$. Biases of the existing liquid cloud parameterizations are summarized in Table 2 and are denoted as "Liq Clouds."

The effects of rain parameterizations are then evaluated and denoted as "Rain" in Table 2. Because Fu et al. (1995) neglects the size dependency of mass extinction coefficient for LW rain and significantly underestimates the optical depth of rain (Figure A2), it underestimates the LW rain effects at the TOA by 0.1 Wm$^{-2}$ and at the surface by 0.37 Wm$^{-2}$. SW rain effects produced from Savijärvi (1997) and the new parameterization are reasonably close.

The global pattern and zonal-mean effects due to updating liquid and rain parameterizations are presented in Figure A5 and as solid red curves in Figure 3 ("Liq Optics"). Changes in the CRE are dominated by clouds. Using the new scheme enhances the CRE, leading to a 1.37 Wm$^{-2}$ increase in upwelling SW fluxes at TOA and a 1.64 Wm$^{-2}$ reduction in net downwelling SW fluxes at the surface. The weaker SW CRE using the new scheme, due to the improved numerical accuracy, helps reduce the brightness of liquid cloud and leads to better agreement with satellite observation (Figure 3 and Table 2, "SW TOA").

The effects of droplets smaller than 4.2 μm on the CRE are further evaluated. It is presented as "Liq Size Range" in Table 2 and shown as red dashed curves in Figure 3. Removing the lower size limits in the radiation enhances the SW CRE at TOA by 0.57 Wm$^{-2}$ and the surface CRE by 0.55 Wm$^{-2}$. Figure A7 further suggests that such effects are strongest in low-level clouds over land. Aside from the effects on annual-mean climatology, the liquid cloud size range is well-known to be important for indirect aerosol effects (Twomey, 1977). Further investigations on the GCM representation of aerosol radiative forcing with the new optics scheme are warranted in the future.

### 4.3. Uncertainties Due To Effective Radius

The parameterization uses $R_e$, or a combination of $R_v$ and $r$, to represent the average over PSD, assuming that optical properties from PSDs that yield the same $R_e$ are identical. In Section 4.1, we expect that optical properties from different shape parameters can be well-explained by $R_e$ (Figures A1, A2, and 5) so that the parameterization generated at $a = 12$ can be used to interact with two-moment microphysics schemes with varying PSDs.

Using the method described in Section 4.2, we estimate the maximum potential biases introduced by this simplification, quantified as the discrepancies in radiative fluxes when $a = 1$ is used instead of $a = 12$. As summarized in Table 2, the choice of shape parameter leads to a 0.5 $\mathrm{Wm^{-2}}$ of global-mean difference in SW fluxes, which is much smaller than biases in existing schemes within the same effective radius range and is comparable to effects from expanded cloud size range.

Although the biases are evaluated using only the Gamma distribution to be consistent with AM4-MG2, the PSD with $a = 1$ is equivalent with an exponential distribution, which places greater weight on smaller particles. In comparison to the log-normal distribution, the Gamma distribution may give less weight to larger particles. However, since large spherical droplets are well-represented by geometric scattering, the uncertainties arising from different size distributions are likely to be minimal. Therefore, given the extreme shape parameters being evaluated, the actual biases due to variations in PSD at the same $R_e$ are expected to be smaller than the estimates presented here.

## 5. Parameterization of Ice Cloud and Snow

The optical properties of ice particles in clouds and precipitation depend on the habit, which is non-spherical and varies greatly (Baum et al., 2005; A. J. Baran, 2009; Korolev & Isaac, 2003; Lawson et al., 2019; Magono & Lee, 1966). Assuming several idealized crystal habits, P. Yang et al. (2013) developed a data set of geometric properties (including maximum dimension ($D$), volume ($V$), and projected area ($A$)) and optical properties (including extinction coefficient ($Q_{ext}$), scattering coefficient ($Q_{sca}$), and asymmetry factor ($g$)) for each crystal habit for the spectral range from 0.2 to 100 μm. This data set is referred to as Yang2013 hereinafter. Following the procedure described in Section 2, these properties are used to generate a parameterization for each habit and roughness condition. Because previous studies have demonstrated that optical properties computed at severely roughened conditions exhibit better agreement with observations (P. Yang et al., 2013), this study presents results based on severely roughened conditions.

Using a Gamma PSD described in Equation 1 of Section 2, optical properties at the native spectral resolution of Yang2013 (Section 2) are converted to the radiation bands of RTE-RRTMGP (Section 3). The shape parameter $a$ is set to be at 1, following Morrison and Gettelman (2008). This choice of $a = 1$, as visualized in Figure 5a, puts more weight on large particles and contributes more by geometric scattering than larger $a$. Optical properties of severely roughened solid columns are generated and presented in Figure 6 as a function of wavenumber and effective radius. More detailed comparisons are presented in Figures A3 and A4, showing that biases due to Pade approximation are negligible. Compared with liquid clouds, ice clouds have a higher SSA in the LW. The spectral variation in mass extinction coefficients of ice is also distinct from liquid (Figure A1 compared to Figure A3).

### 5.1. Effects of Crystal Habit on Effective Radius

It is important to note that the effective radius, $R_e$, of ice crystals cannot be fully resolved by most microphysics schemes used in current GCMs, because they cannot fully resolve the habit of ice crystals. For a given in-cloud ice mass and number concentration generated by a microphysics scheme, the mean equivalent radius of a solid sphere $R_v$ can be computed using Equation 9, by assuming a bulk ice density of 917 $\mathrm{kgm^{-3}}$ (Baum et al., 2011). While $R_v$ is independent of the actual particle density or crystal habit, Figure 7a demonstrates that the size of $r \equiv R_e/R_v$ can vary up to three times depending upon the choice of habit (given the same $R_v$ with the same Gamma PSD, $a = 1$). The $r$ is larger for compact particles, such as droxtal and solid columns, and smaller for less compact particles, such as solid bullet rosette and heavily aggregated plates. For spherical particles, the most compact solid geometry, $r = 1.651$ can be inferred from Equation 14 using $a = 1$.
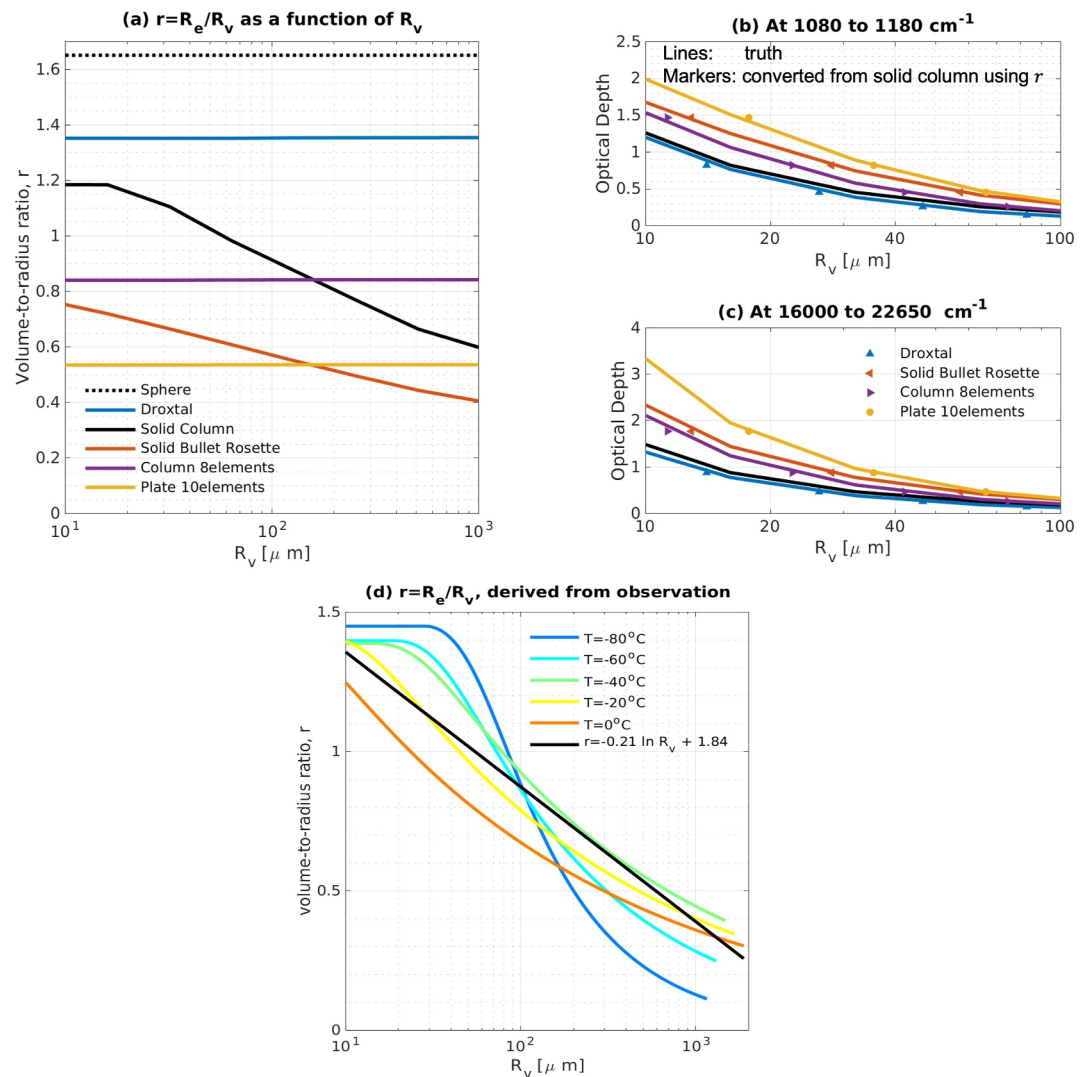
**Figure 7.** (a) The volume-to-radius ratio, $r$, as a function of $R_v$ for idealized crystal habits as marked by color, based on Yang2013 and Gamma particle size distribution (PSD) with $a = 1$. Optical depth of various crystal habits (assuming $10\ \mathrm{g\,m^{-2}}$ of condensate water path) at the same $R_v$, in longwave (b) and shortwave (c). Solid lines are the optical depths of given habits generated using Yang2013, and markers are optical depths inferred from solid columns at the same $R_e$. (d) The volume-to-radius ratio, $r$, as a function of $R_v$ for varying temperature, based on the mass-dimension and area-dimension relationship developed in Heymsfield et al. (2013) and Gamma PSD with $a = 1$. The black curve represents a simplified relationship between $r$ and $R_v$ for general circulation model parameterization.

Consequently, given identical ice mass and number concentration, $R_e$ can vary significantly across the choice of crystal habit. Compact particles tend to have a smaller $R_e$ and projection area, leading to weaker trapping in the LW and more reflection in the SW at the same $R_v$. Figures 7b and 7c shows that with the $10\ \mathrm{g\,m^{-2}}$ of condensate water path and the same number concentration ($R_v$), the optical depths of various habits can be different by up to three times in the infrared window (panel b) and the peak of solar spectrum (panel c). It suggests that if ice crystals are assumed to be spherical due to limitations in representing crystal habit, cloud optical depth can be significantly overestimated due to biases in $R_e$.

Based on Yang2013, the sensitivity of optical properties on crystal habit is relativity small at the same $R_e$. Markers in Figures 7b and 7c show that the optical depths of various habits (lines) are well explained by that of solid columns at the same $R_e$ (markers). The differences are within 10 % for all size ranges (Figure A4) and spectral

ranges (Figure A3). Figure 6 further provides detailed comparisons of the mass extinction coefficient, SSA, and asymmetry factor of heavily aggregated plates ("Plate10ele") (P. Yang et al., 2013). Heavily aggregated plates are used as an example because they show the most significant differences in mass extinction coefficient at $R_v$ when compared to solid columns. Figure 6 suggests that the mass extinction coefficient and SSA as functions of wavenumbers and $R_e$ are very similar between heavily aggregated plates and solid columns. We also find that the asymmetry factor of heavily aggregated plates is higher than solid columns, potentially leading to stronger LW and SW CRE and an increase in net atmospheric absorption, based on Figure 2. This arises from sensitivity of phase function to aspect ratio (Fu, 2007) and multiple scattering within aggregated crystals (A. J. Baran, 2009).

Although the sensitivity of asymmetry factor to habit may affect the CRE and is further evaluated in Section 5.2, the mass extinction coefficient controls the CRE via optical depth when clouds are not fully opaque (Figure 2). Comparisons between solid columns and heavily aggregated plates in Figures A3 and A4 (left panels) show good agreement over most wavelengths, aside from the mid-infrared for small $R_e$. Figure 7b demonstrates that the optical depths of various habits from P. Yang et al. (2013) in the 1,080–1,180 cm$^{-1}$ infrared window (curves, the spectral range where the cloud effects are significant and the differences are largest) can be well reproduced by those of the solid columns at the same $R_e$ (markers). The 10 to 100 µm ranges are shown in Figures 7b and 7c to highlight potential differences caused by the approximation at $R_e$. Overall, these results support the idea that $R_e$ is suitable for a first-order representation of optical depth of ice clouds—for different habits and habit mixtures— when the volume-to-radius ratio $r \equiv R_e/R_v$ is known.

Therefore, when interacting with microphysics schemes that do not resolve the crystal habit, it is important to develop a reasonable representation of $r$ in the radiation treatment of ice clouds and snow (large size falling ice). Based on in-situ observations from 11 aircraft campaigns, Heymsfield et al. (2013) derived the mass-dimension relationship ($m(D)$) and area-dimension relationship ($A(D)$) for ice particles in clouds observed between −86°C to 0°C. Here we convert the mass-dimension relationship to the volume-dimension relationship, using the bulk density of ice at 917 kgm$^{-3}$, following the definition in Equation 9. One caveat is that the relationships derived in Heymsfield et al. (2013) lead to unrealistic area-dimension relationships when the particle size is small ($D$ below 45 µm (Heymsfield et al., 2013)); in this case, the volume is adjusted to that of a sphere. By integrating the derived mass and volume corresponding to a set of particle maximum dimension ($D$) over the PSD, we obtain $r$ and show it as a function of $R_v$ for temperatures at −80°C, −60°C, −40°C, −20°C, and 0°C in Figure 7d.

Figure 7d suggests that the volume-to-radius ratio $r$ decreases dramatically with $R_v$. A decreasing $r$ means that the $R_e$ of ice crystals varies weakly with particle mass compared to $R_v$. This is potentially because heavy ice crystals require a large surface area (i.e., small $r$) to maintain a relatively low fall speed to stay aloft in the air and are consistent with the in-situ observations as they find an increasing proportion of aggregated crystals at large particle size (Cotton et al., 2013).

Due to the limitation in the mass-dimension relationship mentioned earlier, $r$ inferred from Heymsfield et al. (2013) at small $R_v$ may be biased high. The maximum $r$ is 1.651, as derived in Equation 14 analytically for spherical particles. $r$ can reach as low as 0.1 for very large particles at cold temperature (−80°C in Figure 7d), which is lower than the minimum $r$ presented in Figure 7 for idealized crystal habit. To account for the variation of $r$ with particle size, here we approximate the volume-to-radius ratio of ice clouds as:

$$r = \begin{cases} 1.651, & 0\mu m < R_v < 2.46\mu m \\ -0.21 \ln(R_v) + 1.84, & 2.46\mu m \leq R_v \geq 3966.8\mu m \\ 0.1, & R_v > 3966.8\mu m \end{cases} \tag{15}$$

To approximate the optical properties of frozen precipitation, $r$ is set at 0.5, which is typical for idealized, aggregated crystals, as shown in Figure 7. A greater $r$ in snowfall than that of large ice cloud crystals is prescribed because snowfall has a much faster fall speed compared to clouds and does not require a large surface area. When being applied to other numerical models, this simple $r$ approximation for ice and snowfall can be modified to be consistent with the assumptions on mass-size relationship of those models, similar to Ren et al. (2023).

To summarize, here we build the ice parameterization based on a single crystal habit, severely roughened solid columns. It is one of the most dominant crystal habits found in-situ observation (Baum et al., 2005) and is used in satellite observational products for ice clouds (C. Liu et al., 2014; Minnis et al., 2020; Platnick et al., 2016). While the observed crystal habit mixture is complex and is hardly described by idealized habits (Cotton et al., 2013; Lawson et al., 2019; H. Yang et al., 2012), we account for crystal habit by using an observationally-derived $r$ relationship (Equation 15) to approximate their effects on effective radius and optical depth, but neglect the potential uncertainties on asymmetry factor. We note that the mass-size relationship is also important for the geometric and optical properties of ice crystals; because the modeled crystal habits (P. Yang et al., 2013) may not fully represent the growth of mass on aggregated crystals with size, as observed in Francis (1995), Francis et al. (1999), and Heymsfield et al. (2013), the uncertainties caused by mixture of aggregated crystals may exceed the estimate presented here, particularly in the mid infrared. By adopting these simplifications, we aim to achieve a general representation of cloud radiative effects of non-spherical ice particles in GCMs that are comparable with satellite observations.

## 5.2. Comparison With Existing Schemes

Similar to Section 4.2, we utilize the offline radiation package to evaluate the direct effects on CRE from the ice parameterization. Figures 6, A3, and A4 present the optical properties of ice generated from the existing parameterizations used in AM4-MG2. AM4-MG2 uses Fu and Liou (1993) and Fu (1996) for its LW and SW properties of ice clouds, respectively, assuming hexagonal ice crystals. Fu et al. (1995) is used for the optical properties of snowfall that are independent of particle sizes, assuming spherical ice crystals.

Except for the mass extinction coefficient of snow, the ice optical properties over the 1,250 to 50,000 wavenumber range are reasonably close between Fu and Liou (1993) and the new scheme. Because the new scheme is designed to match with user-specified gas optics bands, it more finely resolves the SW spectral dependency of the optical properties (i.e., middle rows of Figure 6). Zonal-mean and global-mean effects on CRE due to updates in the ice cloud parameterization are presented in Figure 3 and Table 2. These results show that differences in the CRE are negligible in the LW. The new scheme produces a stronger SW CRE at the TOA and the surface, because Fu (1996) tends to produce a weaker mass extinction coefficient, higher SSA, and higher asymmetry factor. These biases could be caused by differences in crystal habits (hexagonal vs. severely roughened solid column), thick-averaging from coarse to finer radiation bands, or numerical methods for generating parameterizations.

For snow optics, a major limitation in the existing parameterization is a lack of size dependence in the mass extinction coefficient. The new scheme overcame this limitation by building up the optical properties as a function of $R_e$ from 2.5 to 5,000 μm seamlessly. Neglecting such size dependence can significantly underestimate the optical depth of snowfall when $R_e$ is less than 2000 μm, as illustrated in left panels of Figures 6, A4, and A3. As a result, applying the new parameterization leads to stronger SW radiative effects from snow ("Snow" in Table 2).

Figures 3 and A6 show the sum of effects of ice cloud and snow parameterizations, where the local and zonal-mean effects are dominated by ice clouds. Overall, applying the new ice parameterization enhances the SW CRE, increasing the net upwelling fluxes at the TOA by 1.88 $\mathrm{Wm}^{-2}$ and the net downwelling at the surface by 0.96 $\mathrm{Wm}^{-2}$. Changes in CRE are maximized in Intertropical Convergence Zone (ITCZ). Because the asymmetry factor at large cloud $R_e$ is lower in the new scheme (bottom row of Figure 6) potentially due to the consideration of surface roughness (P. Yang et al., 2013), the SW atmospheric cloud absorption is reduced by 0.88 $\mathrm{Wm}^{-2}$ (bottom panel of Figure 2 shows that smaller asymmetry factor leads to less absorption).

Because SW atmospheric absorption is sensitive to the asymmetry factor (Figure 2 bottom panels) and insensitive to optical depth or cloud water content, we found that biases in SW ATM CRE compared to CERES EBAF in the tropics can be greatly improved by updating the ice optics scheme, which is more consistent with CERES cloud algorithm (Minnis et al., 2020; P. Yang et al., 2008). It also enhances the SW TOA CRE in the ITCZ by up to 5 $\mathrm{Wm}^{-2}$, which reduces biases in these regions (Figure 3 of Zhao et al. (2018a) and Figure 9 of Guo et al. (2024)). However, this improvement of ice cloud effects amplifies the global-mean biases of SW TOA CRE (Table 2 and Figure 3), which is mainly introduced by the excessive cloud water (Guo et al., 2024; Zhao et al., 2018a).
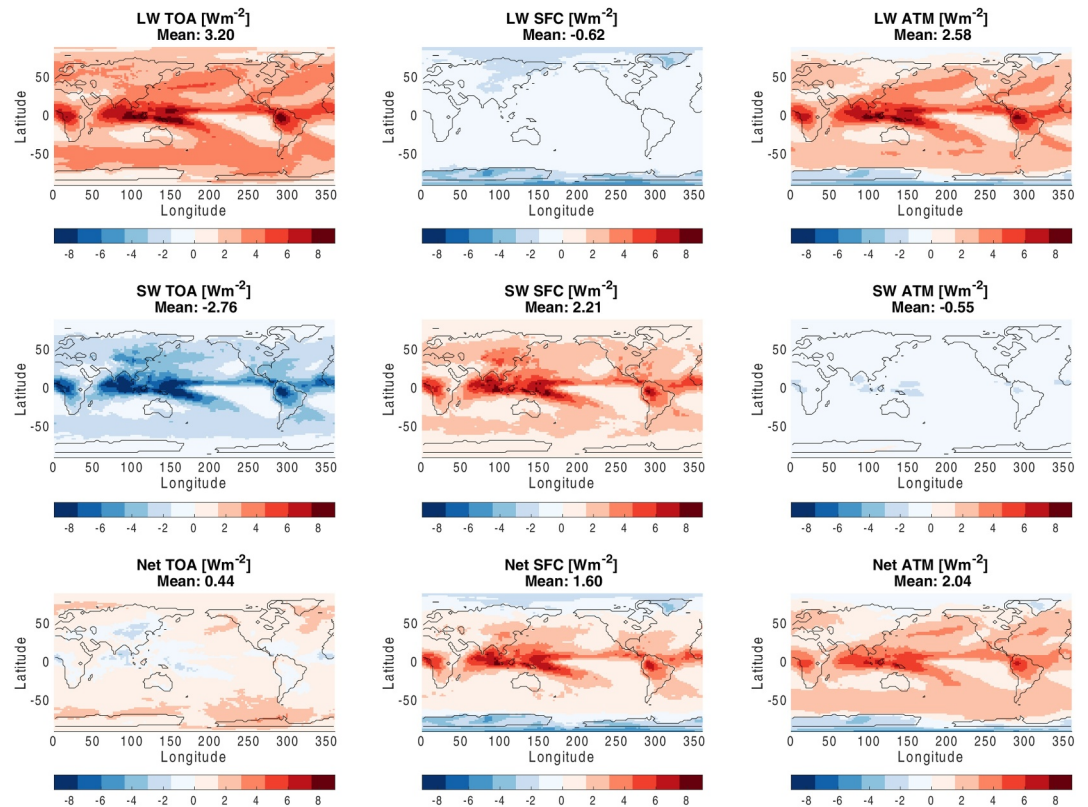
**Figure 8.** Similar to Figure 3, spatial distribution of differences in annual-mean offline CRE caused by adopting the non-spherical ice effective radius adjustment proposed in Equation 15 in comparison with the spherical assumption. It corresponds to the "Nonspherical Ice $R_e$" in Figure 3 and Table 2.

## 5.3. Effects From Nonspherical Effective Radius and Uncertainties

Equation 10 is applied to infer the effective radius $R_e$ of non-spherical ice crystals, rather than directly applying the spherical $R_e$ generated from AM4-MG2. The simple volume-to-radius conversion in Equation 10 shows that less compact crystals are much more reflective (per unit mass) than compact crystals in the SW and more absorptive in the LW (Figure 7). Utilizing this simple non-spherical ice $R_e$ approximation reduces the $R_e$ generated from AM4-MG2 by 20% to 70 %, leading to a significant enhancement of both the LW and SW CRE (as presented in Figures 3 and 8).

At the TOA, using the non-spherical $R_e$ approximation reduces the upwelling LW flux by 3.2 Wm$^{-2}$, improving the biases in LW TOA CRE (3.76 Wm$^{-2}$ in AM4-MG2, Table 2). It enhances the SW TOA CRE by 2.76 Wm$^{-2}$, helping reduce biases in ITCZ (Figure 3 of Zhao et al. (2018a)). The non-spherical $R_e$ approximation increases the LW ATM absorption by 2.58 Wm$^{-2}$ and decreases the SW ATM absorption by 0.55 Wm$^{-2}$. The effect on SW ATM absorption is small because the changes in surface fluxes and TOA fluxes cancel out. It indicates over 6 Wm$^{-2}$ increase in the net surface fluxes over the ITCZ and by 1.6 Wm$^{-2}$ for the global mean (Figure 8 and Table 2).

Moreover, the potential uncertainties caused by the single habit assumption (severely roughened solid column) are estimated using the offline radiation package, as shown by "Habit" in Table 2, Figures 3 and A9. Because the aggregated plates appear to have a higher asymmetry factor (i.e., third compared to the second column in Figure 6), it produces a weaker CRE (increased upwelling LW fluxes at the TOA and downwelling SW fluxes at surface, reduced upwelling SW fluxes), leading to reduced cloud absorption by 0.44 Wm$^{-2}$ compared with solid columns.

Compared with effects from nonspherical $R_e$, the results suggest that when adopting the proposed $r$ parameterization to overcome biases induced by spherical ice assumption, radiative fluxes can be over-corrected. This evaluation is based on optical properties of idealized crystal models built upon P. Yang et al. (2013) and Baum et al. (2014), which may not represent the realistic mass-area-size relationship that are important to single-scattering properties. However, we note that the evaluation provides a reasonable estimate of biases caused by differences between heavily aggregated habits, and we expect weaker effects from a realistic habit mixture. Considering even the maximum estimate of biases is less than half of that induced by biases in $R_e$ due to neglecting habit, it is reasonable to suggest that including a realistic and robust representation of $R_e$ (or $r$), as proposed in Equation 15, is more important to the CRE in GCMs.

## 6. Summary and Discussion

This study develops a traceable and accurate approach to parameterize the optical properties of water condensate (liquid clouds, rain, ice clouds, and snow) for GCM implementations. This approach includes an offline workflow that generates the parameterizations on user-specified radiation bands with a user-specified PSD, as described in Section 2. This two-step workflow is designed so that the proposed parameterization can be easily adapted by GCMs with different radiation codes and microphysics schemes. It also generates high spectral resolution look-up tables that has been used for hyperspectral sounding and has found to produce reasonable radiative closure with satellite and ground-based observation in the mid-infrared (Feng et al., 2021; L. Liu et al., 2025, etc.).

Specifically, the new scheme (a) provides parameterizations at user-defined spectral bands, eliminating the need for online conversions from cloud bands to gas bands and improving the accuracy and computation efficiency; (b) provides consistent optics for liquid clouds and rain, ice clouds and snow over wide ranges, addressing biases introduced by limited size/spectral coverage or lack of size/spectral dependence (see right columns of Figures 4 and 6); and (c) accounts for variations in PSD and crystal habit with an effective radius parameterization based on a volume-to-radius ratio $r$, when effects of these variations on effective radius are not fully resolved by microphysics. Tests with an offline radiation package, driven by 3-hourly fields from a 1-year AM4-MG2 simulation, confirm that these improvements induce effects that are substantial compared to the known spread of CRE among the CMIP6 models (Wild, 2020). For example, the new liquid optics improves SW CRE in TOA by 1.37 Wm$^{-2}$ (Table 2). The use of severely roughened ice crystal properties (P. Yang et al., 2013), consistent with the CERES cloud algorithm, reduces biases in shortwave atmospheric absorption. Additionally, using $r$ to account for non-spherical ice clouds further enhances the CRE in both the LW and SW bands. Although these changes improve the SW CRE in ITCZ, the global mean bias in SW TOA CRE can become more pronounced due to excessive thick clouds in the simulation (Guo et al., 2024; Zhao et al., 2018a). Nonetheless, applying an optics parameterization that aligns more closely with the CERES algorithm helps to identify the causes of model–observation discrepancies and guides future improvements in cloud representations.

The volume-to-radius ratio $r$ is used to represent effects on effective radii ($R_e$) from non-spherical ice crystals (Equation 15) and varying PSDs (Equation 14). For liquid droplets, a broader PSD leads to a higher $r$ (Figure 5). It also means that when the PSD broadens, often a result of increased droplet concentration (Morrison & Gettelman, 2008), the increase in liquid cloud brightness is not as pronounced as one might expect based solely on changes in $R_v$ (Equation 9), due to the partial compensating effect from $r$. Such effects have been taken into account by many earlier studies (Lohmann & Roeckner, 1996; Martin et al., 1994; Morrison & Gettelman, 2008). For ice crystals, $r$ describes the geometry of ice particles. More round and compact particles are associated with larger $r$ and $R_e$, inducing a stronger CRE than for particles that occupy a larger surface area. It is also associated with the terminal velocity of the particles (Heymsfield et al., 2013), such that larger particles in ice clouds require a small $r$ so not to be precipitated out. Consequently, when $R_v$ increases, $R_e$ does not increase at the same rate. This relationship between particle size and $r$ is described by a simple equation in Equation 15 derived from in-situ aircraft campaigns (Heymsfield et al., 2013), without specific assumptions on the crystal habit mixture model or particle density. While it is most ideal to ensure microphysics scheme generates the effective radius of crystal via mass-dimension and area-dimension relationship (A. Baran & Francis, 2004; A. J. Baran et al., 2024; Eidhammer et al., 2017; Milbrandt et al., 2021), rather than via prescribed particle density, the proposed $r$ relationship can be used to overcome biases in existing GCMs and can be easily adapted or tuned for

consistency and energy balances within an individual GCM. Nevertheless, while the proposed $r$ approximation is a simplification of mass-size relationship for GCM parameterization, it can be greatly improved to achieve a consistency with microphysics models used for various applications. The consistencies in definitions and assumptions are particularly important when comparing the effective radius and cloud radiative effects simulated by climate models with satellite observations that also involve an explicit assumptions on mass-size relationship (Cazenave et al., 2019; Minnis et al., 2020, etc.).

With $r$, the new scheme continues to use effective radius ($R_e$) as the main interface between radiation and microphysics—an approach long adopted by GCMs to manage numerical constraints and simplified microphysics. Despite its simplicity, it has proven reliable for representing multi-moment microphysics effects because optical depth depends more strongly on $R_e$ than on PSD or crystal habit (Figures 5 and 7). Consequently, a straightforward representation of CRE in GCMs can be achieved by assuming that optical properties at a given $R_e$ remain valid across different PSDs and habits. We assess the potential biases of this assumption by contrasting small versus large gamma PSD shape parameters for liquid droplets, and heavily aggregated plates versus solid columns for ice crystals (Table 2, Figures 3, 5, 7, A8, and A9). While liquid PSD induces relatively small effects on the CRE, crystal habits remain a known source of uncertainty in the CRE, because the asymmetry factor is sensitive to crystal geometry, orientation, and surface roughness, and may not well represented by effective radius (A. J. Baran, 2009; Francis, 1995; Fu, 2007; Key et al., 2002; Loeb et al., 2018; van Diedenhoven, 2018; P. Yang et al., 2013; Yi et al., 2013; Yi, 2022). Uncertainties in crystal optics can be further elaborated using more realistic crystal habit and habit mixture models (A. J. Baran & Labonnote, 2007; Baum et al., 2014; A. J. Baran et al., 2016; Key et al., 2002; C. Liu et al., 2014), or by using aspect ratio and other geometric parameters to construct parameterizations for the asymmetry factor (Fu, 2007; P. Yang & Fu, 2009; van Diedenhoven et al., 2014). Nevertheless, when applying more advanced ice optics schemes in GCM, accounting for crystal habit effects on effective radius in a manner consistent with the microphysics scheme is still the most important consideration.

Finally, the accuracy of parameterization relies on inputs of refractive indices for spherical particles and optical properties of non-spherical particles. An important potential cause of uncertainty is the temperature dependence of refractive indices (Iwabuchi & Yang, 2011; Rowe et al., 2020), which affects the spectral dependency of the optical properties and is found to be particularly important to microwave (Ding et al., 2017). It is also challenging to achieve radiative closure with remote sensing across different spectral ranges (A. Baran & Francis, 2004; Bantges et al., 2020), potentially due to uncertainties in thermodynamic properties and habit distributions when applying database constructed for individual habits. Alternatively, A. J. Baran and Labonnote (2007) builds an ensemble model and incorporates microphysics assumptions on size and habit distribution when constructing the optical properties; it is found to achieve good radiative closure with instruments at different wavelengths (A. J. Baran, Cotton, et al., 2014). With these limitations, although the parameterization proposed in this study accurately describes the spectral variations of optical properties as given by input data sets, it shall be used with caution for remote sensing. We encourage readers to make use of the open-source code to develop optical parameterizations with alternative input data sets and for other types of hydrometeors.

## Appendix A: Supplementary Figures
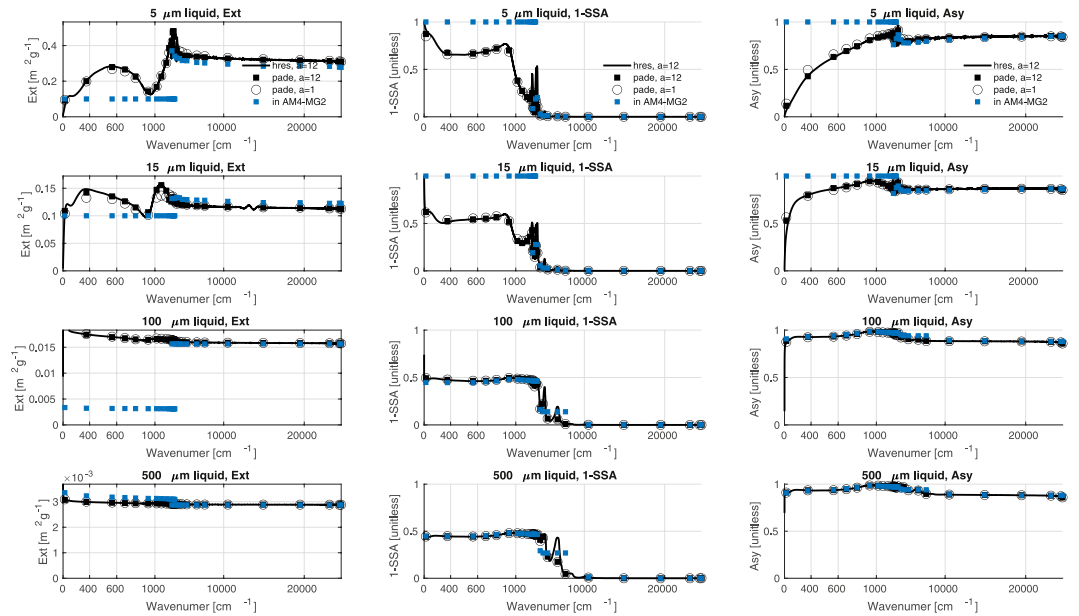


**Figure A1.** Optical properties of droplets as a function of wavenumber [cm$^{-1}$] for effective radius ($R_e$) at 5, 15, 100, and 500 μm, with Gamma shape parameter $a$ at 12. Left: $\bar{\beta}_{R_e,v}$ in curves and $\tilde{\beta}_i(R_e)$ in solid markers [m$^2$g$^{-1}$] in logarithmic scale. Middle: $1 - \bar{\omega}_{R_e,v}$ in curves and $1 - \tilde{\omega}_i(R_e)$ in solid markers. Right: $\bar{g}_{R_e,v}$ in curves and $\tilde{g}_i(R_e)$ in solid markers. Results inferred from parameterization using $a = 1$ are shown in circles. Blue markers are existing parameterizations used in AM4-MG2 (Guo et al., 2021) that are averaged from parameterized bands to gas radiation bands used in RTE-RRTMGP following Edwards and Slingo (1996), based on Held et al. (1993) and Slingo (1989) for longwave and shortwave liquid clouds (4.2–16.6 μm), Fu et al. (1995) and Savijärvi (1997) for longwave and shortwave raindrops (16.6–5,000 μm), respectively.
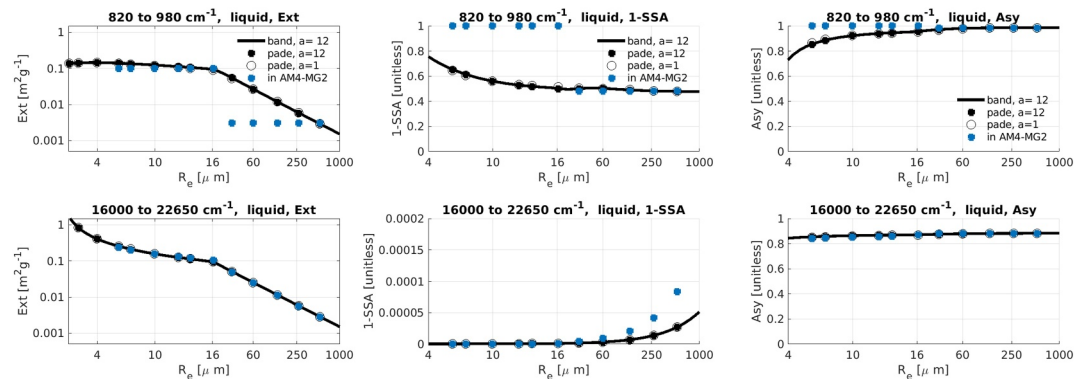


**Figure A2.** The same as Figure A1 but as a function of effective radius $R_e$ [μm] for wavenumber at 1,080–1,180 cm$^{-1}$ (upper panels, infrared window) and at 16,000–22,650 cm$^{-1}$ (lower panels, the peak of solar spectrum). Curves are $\bar{\beta}_{R_e,i}$, $1 - \bar{\omega}_{R_e,i}$, and $\bar{g}_{R_e,i}$ with $a = 12$. Solid black markers and circles are parameterized results for $a = 12$ and $a = 1$, respectively.
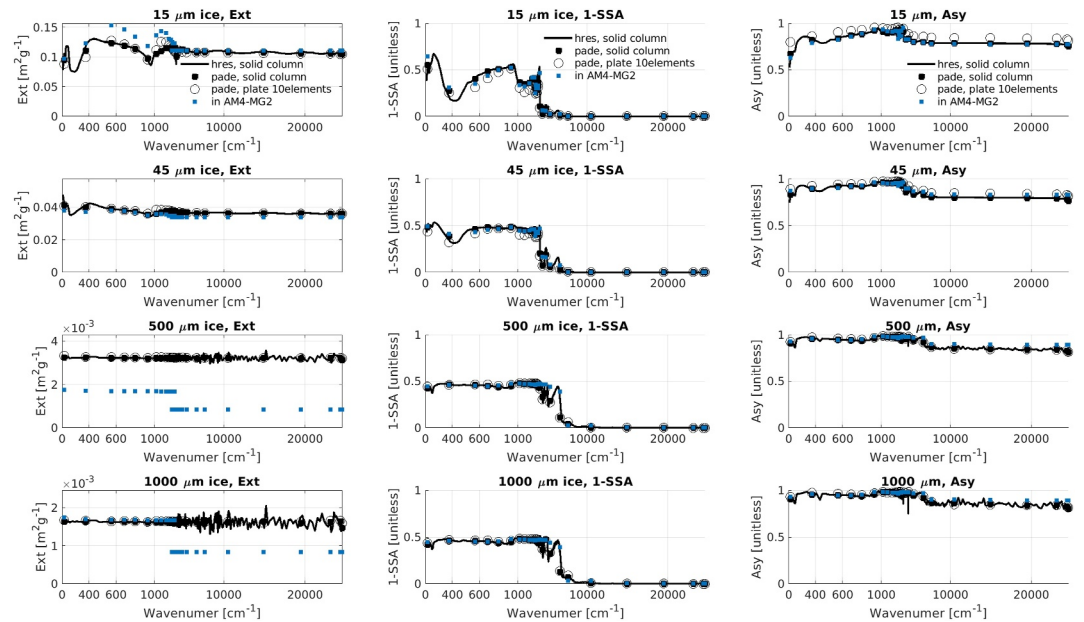
**Figure A3.** Similar to Figure A1 but for effective radii of severely roughened ice crystals at 15, 45, 500, and 1,000 μm. Black curves and solid markers are based on solid columns and circles are based on aggregated plates. The shape parameter ($a$) of the Gamma particle size distribution is 1. Blue markers are existing parameterization used in AM4-MG2 (Guo et al., 2021), based on Fu and Liou (1993) and Fu (1996) for longwave and shortwave ice clouds (9.3–65.1 μm), respectively. Fu et al. (1995) is used for ice precipitation (60–1,800 μm).
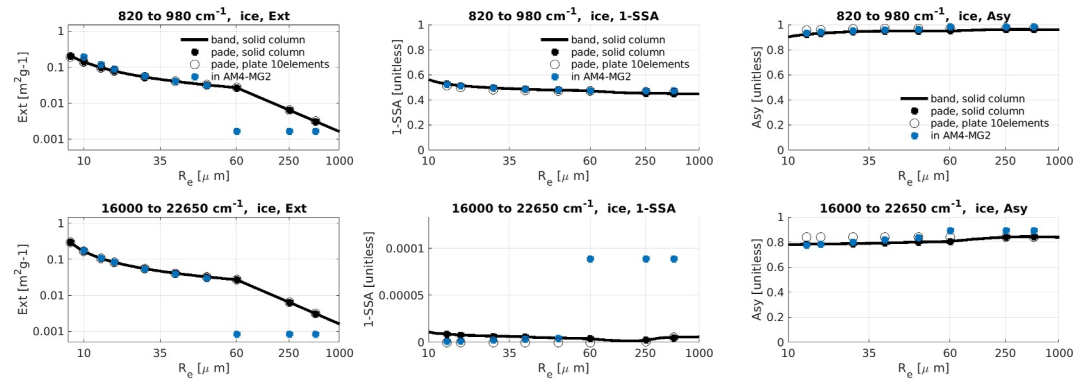


**Figure A4.** Similar to Figure A2 but for ice, with $a = 1$ in the Gamma particle size distribution.
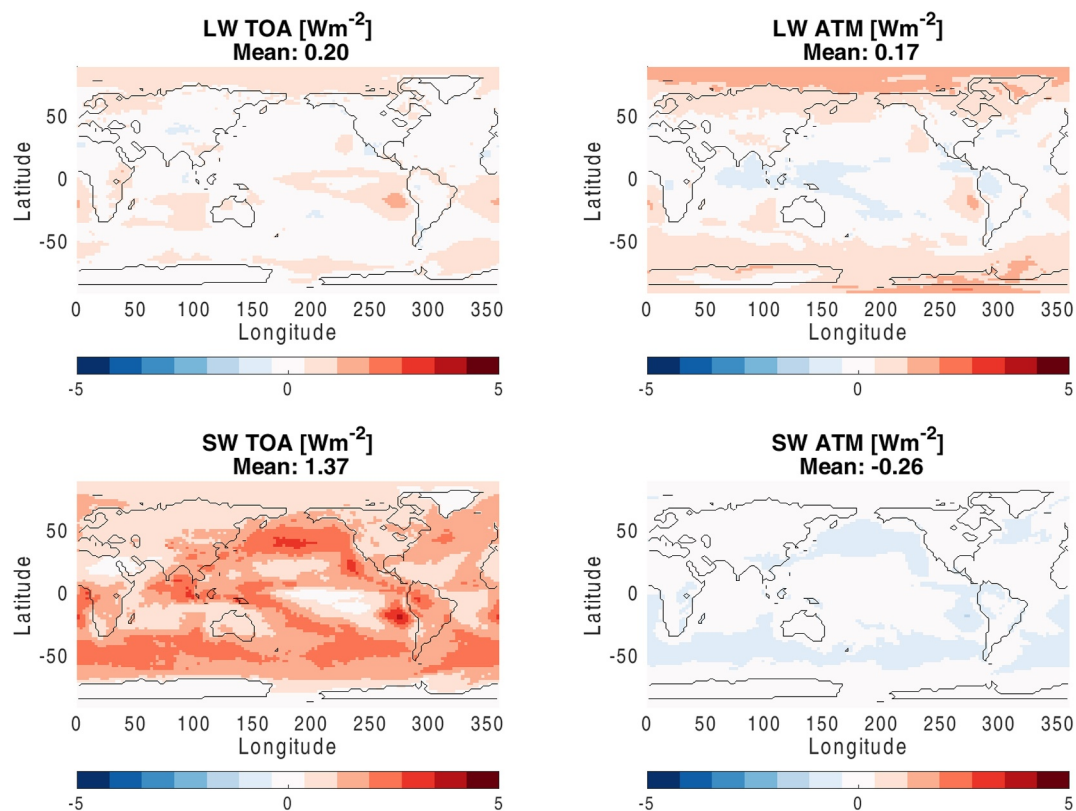
**Figure A5.** Differences in annual-mean offline CRE when using the new liquid parameterization ($a = 12$) to replace the existing parameterizations used in AM4-MG2, while adopting identical liquid cloud size ranges (4.2–16.6 μm). It corresponds to the sum of "Liq Clouds" and "Rain" in Figure 3 and Table 2.
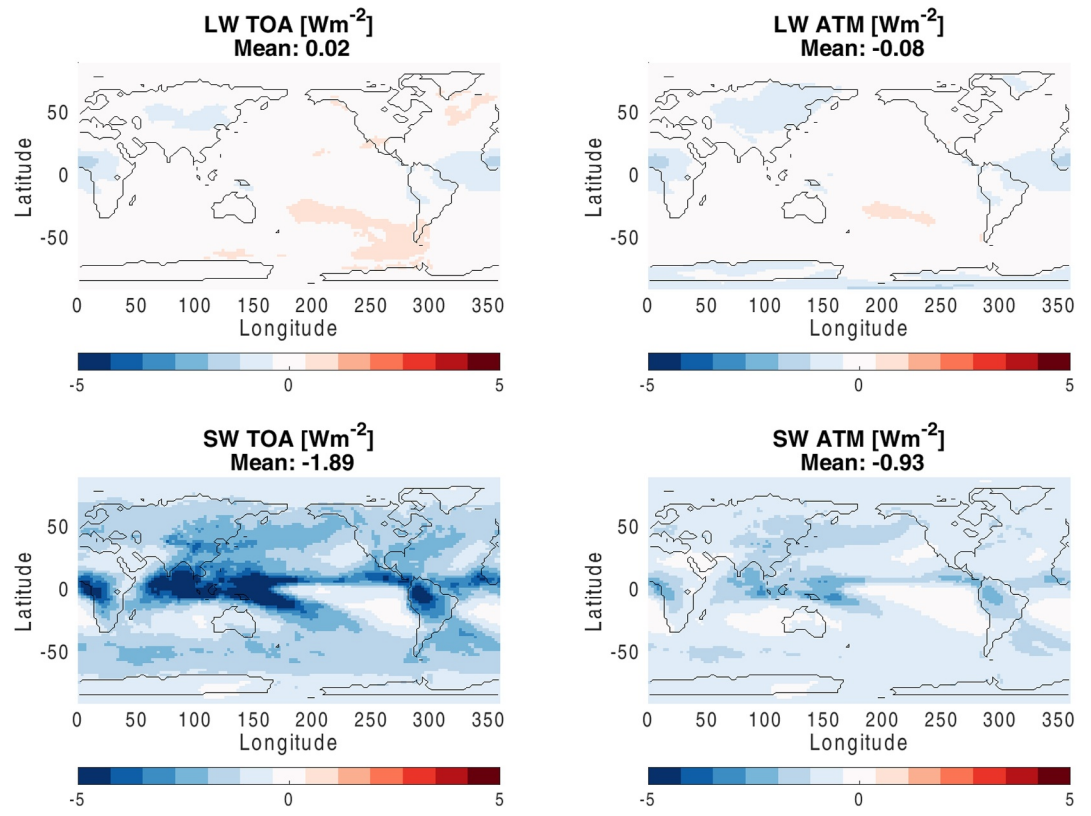
**Figure A6.** Same as Figure A5 but for ice clouds and snow, using new ice parameterization generated from severely-roughed solid column at $a = 1$. It corresponds to the sum of "Ice Clouds" and "Snow" in Figure 3 and Table 2.
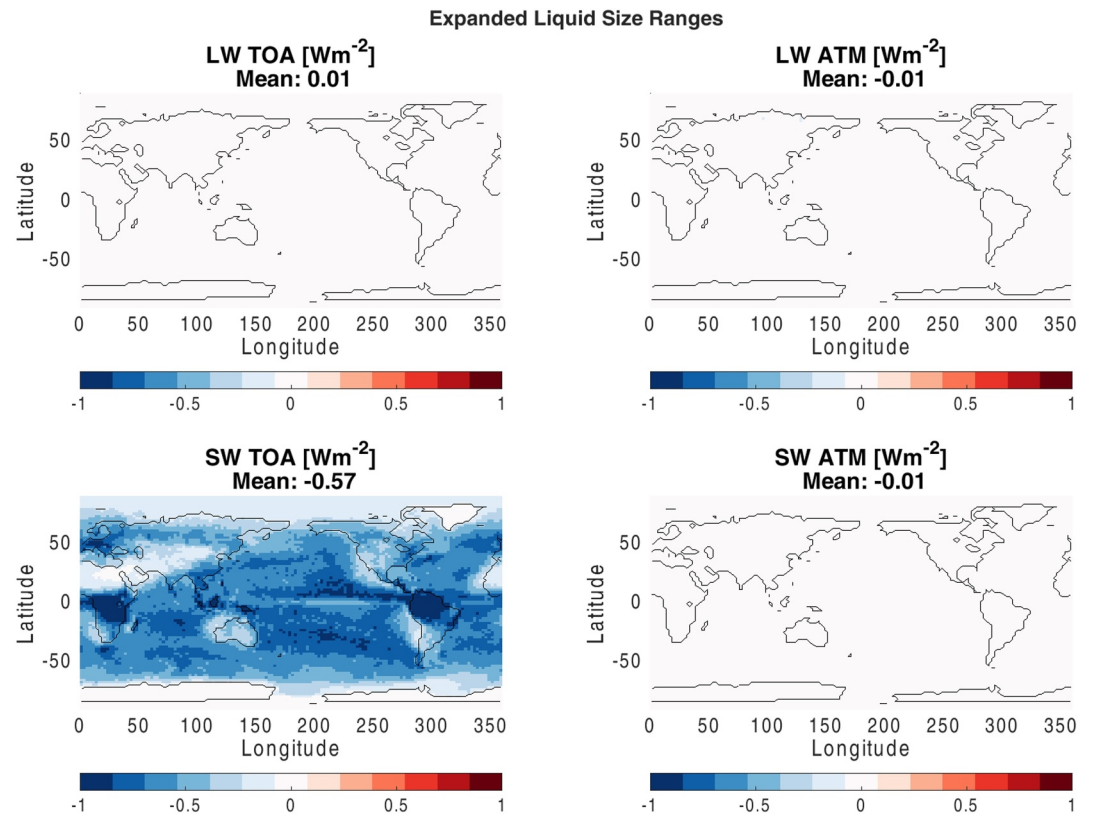
**Figure A7.** Differences in the annual-mean offline CRE when using the new liquid parameterization ($a = 12$) due to expanding liquid size range from [4.2 16.6] μm to [1 100] μm. It corresponds to the "Liq $R_e$ Range" in Figure 3 and Table 2. Effects on LW the top of the atmosphere, LW ATM, and SW ATM are negligible.
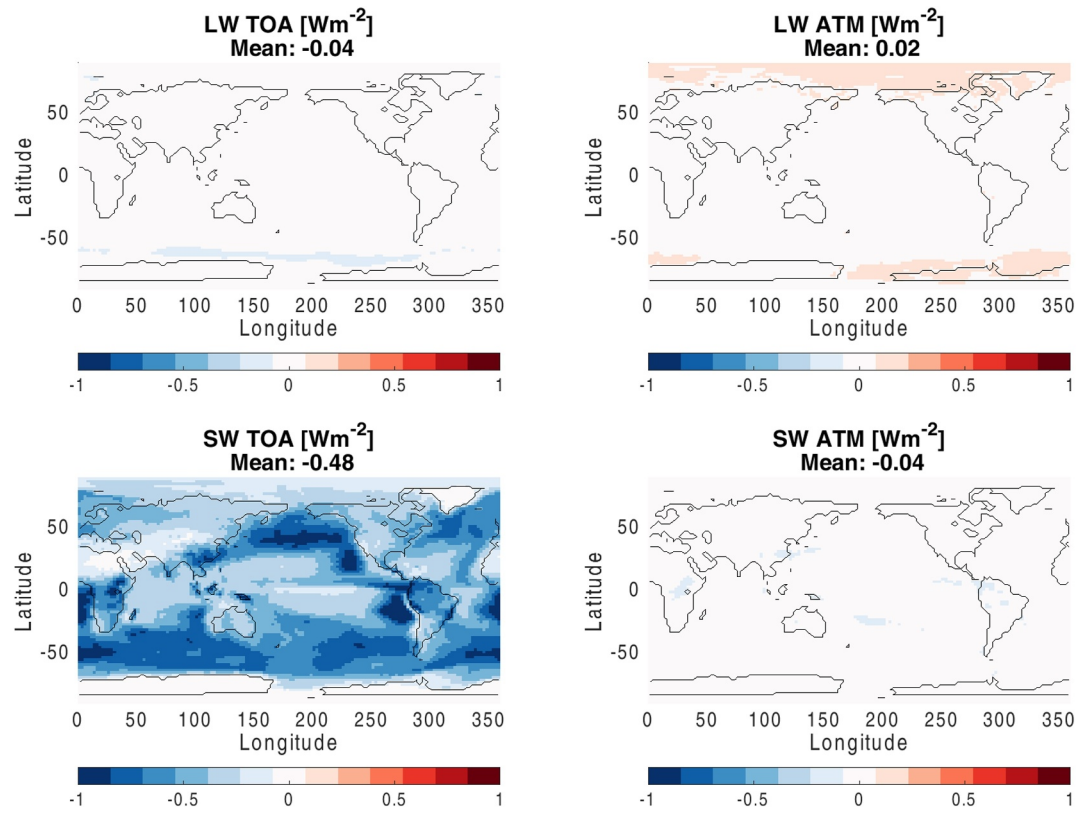
**Figure A8.** Same as Figure A5 but for changes induced by replacing shape parameter $a = 12$ by $a = 1$. It represents a maximum estimate of potential biases caused by particle size distribution. It corresponds to the "PSD" in Figure 3 and Table 2.
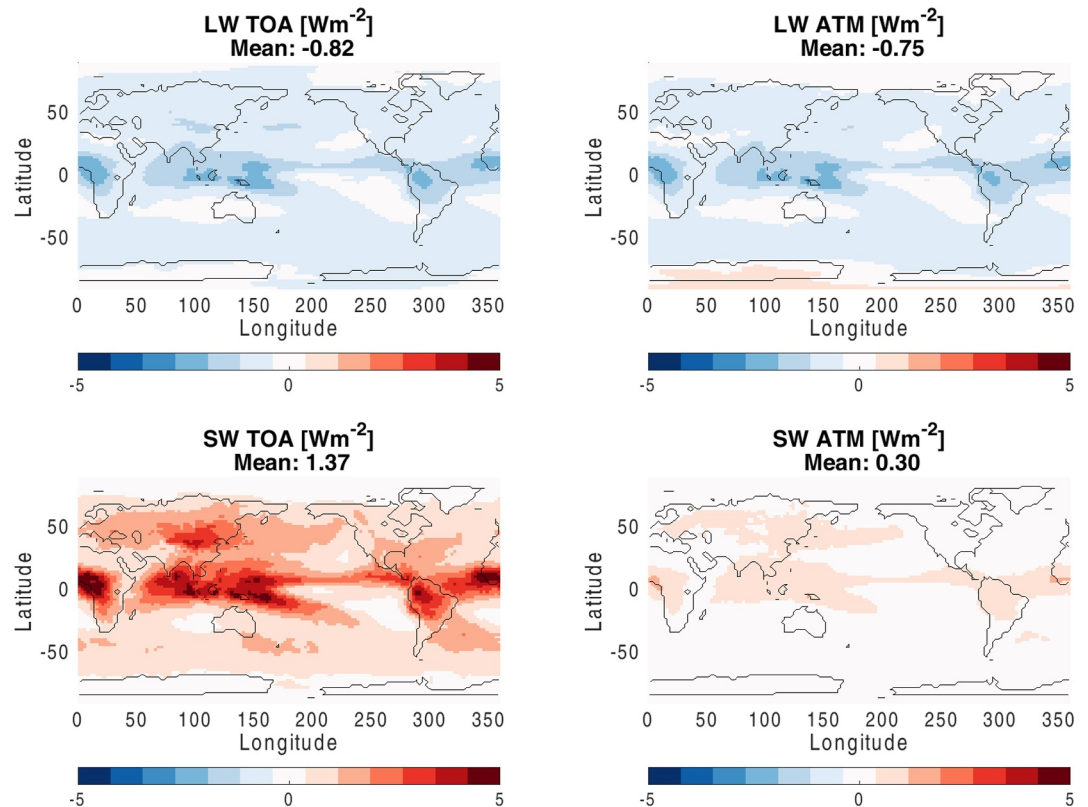
**Figure A9.** Same as Figure A5 but for changes induced by heavily aggregated plates ("Plate10ele," Yang2013), representing a maximum estimate of potential biases caused by crystal habit. It corresponds to the "Habit" in Figure 3 and Table 2.

## Data Availability Statement

A Python package for generating optics parameterizations to user specifications is provided at https://github.com/GRIPS-code/cloud_rad_scheme (Feng & Menzel, 2024) and https://doi.org/10.5281/zenodo.13854891. Example codes that use the parameterizations in Python, Fortran, and Matlab are also provided. Yang et al. (2013) are accessed at https://zenodo.org/records/5348402#.Y3v39-zML6g.

## References

Baker, G. A., Jr., & Gammel, J. L. (1961). The Padé approximant. *Journal of Mathematical Analysis and Applications*, *2*(1), 21–30. https://doi.org/10.1016/0022-247x(61)90042-7

Bantges, R. J., Brindley, H. E., Murray, J. E., Last, A. E., Russell, J. E., Fox, C., et al. (2020). A test of the ability of current bulk optical models to represent the radiative properties of cirrus cloud across the mid-and far-infrared. *Atmospheric Chemistry and Physics*, *20*(21), 12889–12903. https://doi.org/10.5194/acp-20-12889-2020

Baran, A., & Francis, P. (2004). On the radiative properties of cirrus cloud at solar and thermal wavelengths: A test of model consistency using high-resolution airborne radiance measurements. *Quarterly Journal of the Royal Meteorological Society: A Journal of the Atmospheric Sciences, Applied Meteorology and Physical Oceanography*, *130*(598), 763–778. https://doi.org/10.1256/qj.03.151

Baran, A. J. (2009). A review of the light scattering properties of cirrus. *Journal of Quantitative Spectroscopy and Radiative Transfer*, *110*(14–16), 1239–1260. https://doi.org/10.1016/j.jqsrt.2009.02.026

Baran, A. J., Cotton, R., Furtado, K., Havemann, S., Labonnote, L.-C., Marenco, F., et al. (2014). A self-consistent scattering model for cirrus. II: The high and low frequencies. *Quarterly Journal of the Royal Meteorological Society*, *140*(680), 1039–1057. https://doi.org/10.1002/qj.2193

Baran, A. J., Hill, P., Furtado, K., Field, P., & Manners, J. (2014). A coupled cloud physics–radiation parameterization of the bulk optical properties of cirrus and its impact on the met office unified model global atmosphere 5.0 configuration. *Journal of Climate*, *27*(20), 7725–7752. https://doi.org/10.1175/jcli-d-13-00700.1

Baran, A. J., Hill, P., Walters, D., Hardiman, S. C., Furtado, K., Field, P. R., & Manners, J. (2016). The impact of two coupled cirrus microphysics–radiation parameterizations on the temperature and specific humidity biases in the tropical tropopause layer in a climate model. *Journal of Climate*, *29*(14), 5299–5316. https://doi.org/10.1175/jcli-d-15-0821.1

Baran, A. J., & Labonnote, L.-C. (2007). A self-consistent scattering model for cirrus. I: The solar region. *Quarterly Journal of the Royal Meteorological Society: A Journal of the Atmospheric Sciences, Applied Meteorology and Physical Oceanography*, *133*(629), 1899–1912. https://doi.org/10.1002/qj.164

Baran, A. J., Manners, J., Field, P., & Hill, A. (2024). A novel new coupled two-moment parametrization for cirrus radiative properties and its impact in a cloud-aerosol resolving model (CASIM). *AIP Conference Proceedings*, *2988*, 080003. https://doi.org/10.1063/5.0183481

Baum, B. A., Heymsfield, A. J., Yang, P., & Bedka, S. T. (2005). Bulk scattering properties for the remote sensing of ice clouds. Part I: Microphysical data and models. *Journal of Applied Meteorology and Climatology*, *44*(12), 1885–1895. https://doi.org/10.1175/jam2308.1

Baum, B. A., Yang, P., Heymsfield, A. J., Bansemer, A., Cole, B. H., Merrelli, A., et al. (2014). Ice cloud single-scattering property models with the full phase matrix at wavelengths from 0.2 to 100 μm. *Journal of Quantitative Spectroscopy and Radiative Transfer*, *146*, 123–139. https://doi.org/10.1016/j.jqsrt.2014.02.029

Baum, B. A., Yang, P., Heymsfield, A. J., Schmitt, C. G., Xie, Y., Bansemer, A., et al. (2011). Improvements in shortwave bulk scattering and absorption models for the remote sensing of ice clouds. *Journal of Applied Meteorology and Climatology*, *50*(5), 1037–1056. https://doi.org/10.1175/2010jamc2608.1

Bodas-Salcedo, A., Webb, M., Bony, S., Chepfer, H., Dufresne, J.-L., Klein, S., et al. (2011). COSP: Satellite simulation software for model assessment. *Bulletin of the American Meteorological Society*, *92*(8), 1023–1043. https://doi.org/10.1175/2011bams2856.1

Cazenave, Q., Ceccaldi, M., Delanoë, J., Pelon, J., Groß, S., & Heymsfield, A. (2019). Evolution of dardar-cloud ice cloud retrievals: New parameters and impacts on the retrieved microphysical properties. *Atmospheric Measurement Techniques*, *12*(5), 2819–2835. https://doi.org/10.5194/amt-12-2819-2019

Chan, M. A., & Comiso, J. C. (2013). Arctic cloud characteristics as derived from modis, calipso, and cloudsat. *Journal of Climate*, *26*(10), 3285–3306. https://doi.org/10.1175/jcli-d-12-00204.1

Chou, M.-D., Lee, K.-T., Tsay, S.-C., & Fu, Q. (1999). Parameterization for cloud longwave scattering for use in atmospheric models. *Journal of Climate*, *12*(1), 159–169. https://doi.org/10.1175/1520-0442-12.1.159

Cotton, R., Field, P., Ulanowski, Z., Kaye, P. H., Hirst, E., Greenaway, R., et al. (2013). The effective density of small ice particles obtained from in situ aircraft observations of mid-latitude cirrus. *Quarterly Journal of the Royal Meteorological Society*, *139*(676), 1923–1934. https://doi.org/10.1002/qj.2058

Ding, J., Bi, L., Yang, P., Kattawar, G. W., Weng, F., Liu, Q., & Greenwald, T. (2017). Single-scattering properties of ice particles in the microwave regime: Temperature effect on the ice refractive index with implications in remote sensing. *Journal of Quantitative Spectroscopy and Radiative Transfer*, *190*, 26–37. https://doi.org/10.1016/j.jqsrt.2016.11.026

Ebert, E. E., & Curry, J. A. (1992). A parameterization of ice cloud optical properties for climate models. *Journal of Geophysical Research*, *97*(D4), 3831–3836. https://doi.org/10.1029/91jd02472

Edwards, J., Havemann, S., Thelen, J.-C., & Baran, A. (2007). A new parametrization for the radiative properties of ice crystals: Comparison with existing schemes and impact in a GCM. *Atmospheric Research*, *83*(1), 19–35. https://doi.org/10.1016/j.atmosres.2006.03.002

Edwards, J., & Slingo, A. (1996). Studies with a flexible new radiation code. I: Choosing a configuration for a large-scale model. *Quarterly Journal of the Royal Meteorological Society*, *122*(531), 689–719. https://doi.org/10.1002/qj.49712253107

Eidhammer, T., Morrison, H., Mitchell, D., Gettelman, A., & Erfani, E. (2017). Improvements in global climate model microphysics using a consistent representation of ice particle properties. *Journal of Climate*, *30*(2), 609–629. https://doi.org/10.1175/jcli-d-16-0050.1

Eriksson, P., Ekelund, R., Mendrok, J., Brath, M., Lemke, O., & Buehler, S. A. (2018). A general database of hydrometeor single scattering properties at microwave and sub-millimetre wavelengths. *Earth System Science Data*, *10*(3), 1301–1326. https://doi.org/10.5194/essd-10-1301-2018

Fan, S., Ginoux, P., Seman, C. J., Silvers, L. G., & Zhao, M. (2019). Toward improved cloud-phase simulation with a mineral dust and temperature-dependent parameterization for ice nucleation in mixed-phase clouds. *Journal of the Atmospheric Sciences*, *76*(11), 3655–3667. https://doi.org/10.1175/jas-d-18-0287.1

Feng, J., Huang, Y., & Qu, Z. (2021). A simulation-experiment-based assessment of retrievals of above-cloud temperature and water vapor using a hyperspectral infrared sounder. *Atmospheric Measurement Techniques*, *14*(8), 5717–5734. https://doi.org/10.5194/amt-14-5717-2021

Feng, J., & Menzel, R. (2024). fengzydy/cloud_rad_scheme: Package for JAMES submission. *Zenodo*. https://doi.org/10.5281/zenodo.13854892

Francis, P. N. (1995). Some aircraft observations of the scattering properties of ice crystals. *Journal of the Atmospheric Sciences*, *52*(8), 1142–1154. https://doi.org/10.1175/1520-0469(1995)052<1142:saoots>2.0.co;2

Francis, P. N., Foot, J. S., & Baran, A. J. (1999). Aircraft measurements of the solar and infrared radiative properties of cirrus and their dependence on ice crystal shape. *Journal of Geophysical Research*, *104*(D24), 31685–31695.

Fu, Q. (1996). An accurate parameterization of the solar radiative properties of cirrus clouds for climate models. *Journal of Climate*, *9*(9), 2058–2082. https://doi.org/10.1175/1520-0442(1996)009<2058:aapots>2.0.co;2

Fu, Q. (2007). A new parameterization of an asymmetry factor of cirrus clouds for climate models. *Journal of the Atmospheric Sciences*, *64*(11), 4140–4150. https://doi.org/10.1175/2007jas2289.1

Fu, Q., Krueger, S. K., & Liou, K. (1995). Interactions of radiation and convection in simulated tropical cloud clusters. *Journal of the Atmospheric Sciences*, *52*(9), 1310–1328. https://doi.org/10.1175/1520-0469(1995)052<1310:ioraci>2.0.co;2

Fu, Q., & Liou, K. N. (1993). Parameterization of the radiative properties of cirrus clouds. *Journal of the Atmospheric Sciences*, *50*(13), 2008–2025. https://doi.org/10.1175/1520-0469(1993)050<2008:potrpo>2.0.co;2

Geer, A., & Baordo, F. (2014). Improved scattering radiative transfer for frozen hydrometeors at microwave frequencies. *Atmospheric Measurement Techniques*, *7*(6), 1839–1860. https://doi.org/10.5194/amt-7-1839-2014

Geer, A. J., Bauer, P., Lonitz, K., Barlakas, V., Eriksson, P., Mendrok, J., et al. (2021). Bulk hydrometeor optical properties for microwave and sub-millimetre radiative transfer in rttov-scatt v13. 0. *Geoscientific Model Development*, *14*(12), 7497–7526. https://doi.org/10.5194/gmd-14-7497-2021

Gettelman, A., & Morrison, H. (2015). Advanced two-moment bulk microphysics for global models. part i: Off-line tests and comparison with other schemes. *Journal of Climate*, *28*(3), 1268–1287. https://doi.org/10.1175/jcli-d-14-00102.1

Goody, R., West, R., Chen, L., & Crisp, D. (1989). The correlated-k method for radiation calculations in nonhomogeneous atmospheres. *Journal of Quantitative Spectroscopy and Radiative Transfer*, *42*(6), 539–550. https://doi.org/10.1016/0022-4073(89)90044-7

Guo, H., Ming, Y., Fan, S., Zhou, L., Harris, L., & Zhao, M. (2021). Two-moment bulk cloud microphysics with prognostic precipitation in GFDL's atmosphere model AM4.0: Configuration and performance. *Journal of Advances in Modeling Earth Systems*, *13*(6), e2020MS002453. https://doi.org/10.1029/2020ms002453

Guo, H., Silvers, L. G., Paynter, D., Dong, W., Fan, S.-M., Jing, X., et al. (2024). Assessing clouds in GFDL's AM4.0 with different microphysical parameterizations using the satellite simulator package COSP. *Authorea Preprints*.

Hansen, J. E., & Pollack, J. B. (1970). Near-infrared light scattering by terrestrial clouds. *Journal of the Atmospheric Sciences*, *27*(2), 265–281. https://doi.org/10.1175/1520-0469(1970)027<0265:nilsbt>2.0.co;2

Held, I. M., Hemler, R. S., & Ramaswamy, V. (1993). Radiative-convective equilibrium with explicit two-dimensional moist convection. *Journal of the Atmospheric Sciences*, *50*(23), 3909–3927. https://doi.org/10.1175/1520-0469(1993)050<3909:rcewet>2.0.co;2

Heymsfield, A. J., Bansemer, A., Field, P. R., Durden, S. L., Stith, J. L., Dye, J. E., et al. (2002). Observations and parameterizations of particle size distributions in deep tropical cirrus and stratiform precipitating clouds: Results from in situ observations in trmm field campaigns. *Journal of the Atmospheric Sciences*, *59*(24), 3457–3491. https://doi.org/10.1175/1520-0469(2002)059<3457:oapops>2.0.co;2

Heymsfield, A. J., & Platt, C. (1984). A parameterization of the particle size spectrum of ice clouds in terms of the ambient temperature and the ice water content. *Journal of the Atmospheric Sciences*, *41*(5), 846–855. https://doi.org/10.1175/1520-0469(1984)041<0846:apotps>2.0.co;2

Heymsfield, A. J., Schmitt, C., & Bansemer, A. (2013). Ice cloud particle size distributions and pressure-dependent terminal velocities from in situ observations at temperatures from 0 to- 86 c. *Journal of the Atmospheric Sciences*, *70*(12), 4123–4154. https://doi.org/10.1175/jas-d-12-0124.1

Hogan, R. J., & Bozzo, A. (2018). A flexible and efficient radiation scheme for the ECMWF model. *Journal of Advances in Modeling Earth Systems*, *10*(8), 1990–2008. https://doi.org/10.1029/2018ms001364

Hu, Y., & Stamnes, K. (1993). An accurate parameterization of the radiative properties of water clouds suitable for use in climate models. *Journal of Climate*, *6*(4), 728–742. https://doi.org/10.1175/1520-0442(1993)006<0728:aapotr>2.0.co;2

Iwabuchi, H., & Yang, P. (2011). Temperature dependence of ice optical constants: Implications for simulating the single-scattering properties of cold ice clouds. *Journal of Quantitative Spectroscopy and Radiative Transfer*, *112*(15), 2520–2525. https://doi.org/10.1016/j.jqsrt.2011.06.017

Kato, S., Rose, F. G., Rutan, D. A., Thorsen, T. J., Loeb, N. G., Doelling, D. R., et al. (2018). Surface irradiances of edition 4.0 clouds and the Earth's radiant energy system (CERES) energy balanced and filled (EBAF) data product. *Journal of Climate*, *31*(11), 4501–4527. https://doi.org/10.1175/jcli-d-17-0523.1

Key, J. R., Yang, P., Baum, B. A., & Nasiri, S. L. (2002). Parameterization of shortwave ice cloud optical properties for various particle habits. *Journal of Geophysical Research*, *107*(D13), AAC-7. https://doi.org/10.1029/2001jd000742

Kleanthous, A., Baran, A. J., Betcke, T., Hewett, D. P., & Westbrook, C. D. (2024). An application of the boundary element method (BEM) to the calculation of the single-scattering properties of very complex ice crystals in the microwave and sub-millimetre regions of the electromagnetic spectrum. *Journal of Quantitative Spectroscopy and Radiative Transfer*, *312*, 108793. https://doi.org/10.1016/j.jqsrt.2023.108793

Korolev, A., & Isaac, G. (2003). Roundness and aspect ratio of particles in ice clouds. *Journal of the Atmospheric Sciences*, *60*(15), 1795–1808. https://doi.org/10.1175/1520-0469(2003)060<1795:raarop>2.0.co;2

Kristjánsson, J., Edwards, J., & Mitchell, D. (1999). A new parameterization scheme for the optical properties of ice crystals for use in general circulation models of the atmosphere. *Physics and Chemistry of the Earth - Part B: Hydrology, Oceans and Atmosphere*, *24*(3), 231–236. https://doi.org/10.1016/s1464-1909(98)00043-4

Lawson, R., Woods, S., Jensen, E., Erfani, E., Gurganus, C., Gallagher, M., et al. (2019). A review of ice particle shapes in cirrus formed in situ and in anvils. *Journal of Geophysical Research: Atmospheres*, *124*(17–18), 10049–10090. https://doi.org/10.1029/2018jd030122

Liu, C., Yang, P., Minnis, P., Loeb, N., Kato, S., Heymsfield, A., & Schmitt, C. (2014). A two-habit model for the microphysical and optical properties of ice clouds. *Atmospheric Chemistry and Physics*, *14*(24), 13719–13737. https://doi.org/10.5194/acp-14-13719-2014

Liu, L., Huang, Y., & Gyakum, J. R. (2025). Clouds reduce downwelling longwave radiation over land in a warming climate. *Nature*, *637*(8047), 1–7. https://doi.org/10.1038/s41586-024-08323-x

Loeb, N. G., Yang, P., Rose, F. G., Hong, G., Sun-Mack, S., Minnis, P., et al. (2018). Impact of ice cloud microphysics on satellite cloud retrievals and broadband flux radiative transfer model calculations. *Journal of Climate*, *31*(5), 1851–1864. https://doi.org/10.1175/jcli-d-17-0426.1

Lohmann, U., & Roeckner, E. (1996). Design and performance of a new cloud microphysics scheme developed for the echam general circulation model. *Climate Dynamics*, *12*(8), 557–572. https://doi.org/10.1007/s003820050128

Macke, A. (1993). Scattering of light by polyhedral ice crystals. *Applied Optics*, *32*(15), 2780–2788. https://doi.org/10.1364/ao.32.002780

Magono, C., & Lee, C. W. (1966). Meteorological classification of natural snow crystals. *Journal of the Faculty of Science, Hokkaido University - Series 7: Geophysics*, *2*(4), 321–335.

Martin, G., Johnson, D., & Spice, A. (1994). The measurement and parameterization of effective radius of droplets in warm stratocumulus clouds. *Journal of the Atmospheric Sciences*, *51*(13), 1823–1842. https://doi.org/10.1175/1520-0469(1994)051<1823:tmapoe>2.0.co;2

Mätzler, C. (2002). Matlab functions for mie scattering and absorption, version 2.

McFarquhar, G. M., & Heymsfield, A. J. (1998). The definition and significance of an effective radius for ice clouds. *Journal of the Atmospheric Sciences*, *55*(11), 2039–2052. https://doi.org/10.1175/1520-0469(1998)055<2039:tdasoa>2.0.co;2

McFarquhar, G. M., Yang, P., Macke, A., & Baran, A. J. (2002). A new parameterization of single scattering solar radiative properties for tropical anvils using observed ice crystal size and shape distributions. *Journal of the Atmospheric Sciences*, *59*(16), 2458–2478. https://doi.org/10.1175/1520-0469(2002)059<2458:anposs>2.0.co;2

Mie, G. (1908). Beiträge zur Optik trüber Medien, speziell kolloidaler Metallösungen. *Annalen der Physik*, *330*(3), 377–445. https://doi.org/10.1002/andp.19083300302

Milbrandt, J. A., Morrison, H., Dawson II, D. T., & Paukert, M. (2021). A triple-moment representation of ice in the predicted particle properties (P3) microphysics scheme. *Journal of the Atmospheric Sciences*, *78*(2), 439–458. https://doi.org/10.1175/jas-d-20-0084.1

Minnis, P., Sun-Mack, S., Chen, Y., Chang, F.-L., Yost, C. R., Smith, W. L., et al. (2020). Ceres modis cloud product retrievals for edition 4—Part I: Algorithm changes. *IEEE Transactions on Geoscience and Remote Sensing*, *59*(4), 2744–2780. https://doi.org/10.1109/tgrs.2020.3008866

Morrison, H., & Gettelman, A. (2008). A new two-moment bulk stratiform cloud microphysics scheme in the community atmosphere model, version 3 (CAM3). part i: Description and numerical tests. *Journal of Climate*, *21*(15), 3642–3659. https://doi.org/10.1175/2008jcli2105.1

Petty, G. W. (2023). *A first course in atmospheric radiation*. Sundog Publishing LLC.

Pincus, R., Hemler, R., & Klein, S. A. (2006). Using stochastically generated subcolumns to represent cloud structure in a large-scale model. *Monthly Weather Review*, *134*(12), 3644–3656. https://doi.org/10.1175/mwr3257.1

Pincus, R., Mlawer, E. J., & Delamere, J. S. (2019). Balancing accuracy, efficiency, and flexibility in radiation calculations for dynamical models. *Journal of Advances in Modeling Earth Systems*, *11*(10), 3074–3089. https://doi.org/10.1029/2019ms001621

Platnick, S., Meyer, K. G., King, M. D., Wind, G., Amarasinghe, N., Marchant, B., et al. (2016). The modis cloud optical and microphysical products: Collection 6 updates and examples from terra and aqua. *IEEE Transactions on Geoscience and Remote Sensing*, *55*(1), 502–525. https://doi.org/10.1109/tgrs.2016.2610522

Ren, T., Yang, P., Garrett, K., Ma, Y., Ding, J., & Coy, J. (2023). A microphysics-scheme-consistent snow optical parameterization for the community radiative transfer model. *Monthly Weather Review*, *151*(2), 383–402. https://doi.org/10.1175/mwr-d-22-0145.1

Rowe, P., Fergoda, M., & Neshyba, S. (2020). Temperature-dependent optical properties of liquid water from 240 to 298 K. *Journal of Geophysical Research: Atmospheres*, *125*(17), e2020JD032624. https://doi.org/10.1029/2020jd032624

Savijärvi, H. (1997). Short-wave optical properties of rain. *Tellus*, *49*(2), 177–181. https://doi.org/10.1034/j.1600-0870.1997.t01-1-00002.x

Savijärvi, H., & Räisänen, P. (1998). Long-wave optical properties of water clouds and rain. *Tellus*, *50*(1), 1–11. https://doi.org/10.3402/tellusa.v50i1.14508

Segelstein, D. J. (1981). *The complex refractive index of water* (Unpublished doctoral dissertation). University of Missouri–Kansas City.

Sieron, S. B., Clothiaux, E. E., Zhang, F., Lu, Y., & Otkin, J. A. (2017). Comparison of using distribution-specific versus effective radius methods for hydrometeor single-scattering properties for all-sky microwave satellite radiance simulations with different microphysics parameterization schemes. *Journal of Geophysical Research: Atmospheres*, *122*(13), 7027–7046. https://doi.org/10.1002/2017jd026494

Sieron, S. B., Zhang, F., Clothiaux, E. E., Zhang, L. N., & Lu, Y. (2018). Representing precipitation ice species with both spherical and nonspherical particles for radiative transfer modeling of microphysics-consistent cloud microwave scattering properties. *Journal of Advances in Modeling Earth Systems*, *10*(4), 1011–1028. https://doi.org/10.1002/2017ms001226

Slingo, A. (1989). A gcm parameterization for the shortwave radiative properties of water clouds. *Journal of the Atmospheric Sciences*, *46*(10), 1419–1427. https://doi.org/10.1175/1520-0469(1989)046<1419:agpfts>2.0.co;2

Slingo, A., & Schrecker, H. (1982). On the shortwave radiative properties of stratiform water clouds. *Quarterly Journal of the Royal Meteorological Society*, *108*(456), 407–426. https://doi.org/10.1002/qj.49710845607

Takano, Y., & Liou, K. (1995). Radiative transfer in cirrus clouds. part III: Light scattering by irregular ice crystals. *Journal of the Atmospheric Sciences*, *52*(7), 818–837. https://doi.org/10.1175/1520-0469(1995)052<0818:rticcp>2.0.co;2

Takano, Y., & Liou, K.-N. (1989). Solar radiative transfer in cirrus clouds. part I: Single-scattering and optical properties of hexagonal ice crystals. *Journal of the Atmospheric Sciences*, *46*(1), 3–19. https://doi.org/10.1175/1520-0469(1989)046<0003:srticc>2.0.co;2

Tang, G., Yang, P., Kattawar, G. W., Huang, X., Mlawer, E. J., Baum, B. A., & King, M. D. (2018). Improvement of the simulation of cloud longwave scattering in broadband radiative transfer models. *Journal of the Atmospheric Sciences*, *75*(7), 2217–2233. https://doi.org/10.1175/jas-d-18-0014.1

Trepte, Q. Z., Minnis, P., Sun-Mack, S., Yost, C. R., Chen, Y., Jin, Z., et al. (2019). Global cloud detection for ceres edition 4 using terra and aqua modis data. *IEEE Transactions on Geoscience and Remote Sensing*, *57*(11), 9410–9449. https://doi.org/10.1109/tgrs.2019.2926620

Twomey, S. (1977). The influence of pollution on the shortwave albedo of clouds. *Journal of the Atmospheric Sciences*, *34*(7), 1149–1152. https://doi.org/10.1175/1520-0469(1977)034<1149:tiopot>2.0.co;2

van Diedenhoven, B. (2018). Remote sensing of crystal shapes in ice clouds. Springer Series in Light Scattering: Volume 2: Light Scattering, Radiative Transfer and Remote Sensing, 197–250. *Springer Series in Light Scattering*, 197–250. https://doi.org/10.1007/978-3-319-70808-9_5

van Diedenhoven, B., Ackerman, A. S., Cairns, B., & Fridlind, A. M. (2014). A flexible parameterization for shortwave optical properties of ice crystals. *Journal of the Atmospheric Sciences*, *71*(5), 1763–1782. https://doi.org/10.1175/jas-d-13-0205.1

Wild, M. (2020). The global energy balance as represented in cmip6 climate models. *Climate Dynamics*, *55*(3), 553–577. https://doi.org/10.1007/s00382-020-05282-7

Wyser, K., & Yang, P. (1998). Average ice crystal size and bulk short-wave single-scattering properties of cirrus clouds. *Atmospheric Research*, *49*(4), 315–335. https://doi.org/10.1016/s0169-8095(98)00083-0

Yang, H., Dobbie, S., Herbert, R., Connolly, P., Gallagher, M., Ghosh, S., et al. (2012). The effect of observed vertical structure, habits, and size distributions on the solar radiative properties and cloud evolution of cirrus clouds. *Quarterly Journal of the Royal Meteorological Society*, *138*(666), 1221–1232. https://doi.org/10.1002/qj.973

Yang, P., Bi, L., Baum, B. A., Liou, K.-N., Kattawar, G. W., Mishchenko, M. I., & Cole, B. (2013). Spectrally consistent scattering, absorption, and polarization properties of atmospheric ice crystals at wavelengths from 0.2 to 100 μm. *Journal of the Atmospheric Sciences*, *70*(1), 330–347. https://doi.org/10.1175/jas-d-12-039.1

Yang, P., & Fu, Q. (2009). Dependence of ice crystal optical properties on particle aspect ratio. *Journal of Quantitative Spectroscopy and Radiative Transfer*, *110*(14–16), 1604–1614. https://doi.org/10.1016/j.jqsrt.2009.03.004

Yang, P., Kattawar, G. W., Hong, G., Minnis, P., & Hu, Y. (2008). Uncertainties associated with the surface texture of ice particles in satellite-based retrieval of cirrus clouds—Part I: Single-Scattering properties of ice crystals with surface roughness. *IEEE Transactions on Geoscience and Remote Sensing*, *46*(7), 1940–1947. https://doi.org/10.1109/tgrs.2008.916471

Yang, P., Liou, K., Wyser, K., & Mitchell, D. (2000). Parameterization of the scattering and absorption properties of individual ice crystals. *Journal of Geophysical Research*, *105*(D4), 4699–4718. https://doi.org/10.1029/1999jd900755

Yi, B. (2022). Diverse cloud radiative effects and global surface temperature simulations induced by different ice cloud optical property parameterizations. *Scientific Reports*, *12*(1), 10539. https://doi.org/10.1038/s41598-022-14608-w

Yi, B., Yang, P., Baum, B. A., L'Ecuyer, T., Oreopoulos, L., Mlawer, E. J., et al. (2013). Influence of ice particle surface roughening on the global cloud radiative effect. *Journal of the Atmospheric Sciences*, *70*(9), 2794–2807. https://doi.org/10.1175/jas-d-13-020.1

Yost, C. R., Minnis, P., Sun-Mack, S., Chen, Y., & Smith, W. L. (2020). Ceres modis cloud product retrievals for edition 4—Part II: Comparisons to cloudsat and calipso. *IEEE Transactions on Geoscience and Remote Sensing*, *59*(5), 3695–3724. https://doi.org/10.1109/tgrs.2020.3015155

Zelinka, M. D., Myers, T. A., McCoy, D. T., Po-Chedley, S., Caldwell, P. M., Ceppi, P., et al. (2020). Causes of higher climate sensitivity in cmip6 models. *Geophysical Research Letters*, *47*(1), e2019GL085782. https://doi.org/10.1029/2019gl085782

Zhang, Y., Macke, A., & Albers, F. (1999). Effect of crystal size spectrum and crystal shape on stratiform cirrus radiative forcing. *Atmospheric Research*, *52*(1–2), 59–75. https://doi.org/10.1016/s0169-8095(99)00026-5

Zhao, M., Golaz, J.-C., Held, I., Guo, H., Balaji, V., Benson, R., et al. (2018a). The GFDL global atmosphere and land model AM4. 0/LM4. 0: 1. Simulation characteristics with prescribed SSTs. *Journal of Advances in Modeling Earth Systems*, *10*(3), 691–734. https://doi.org/10.1002/2017ms001208

Zhao, M., Golaz, J.-C., Held, I., Guo, H., Balaji, V., Benson, R., et al. (2018b). The GFDL global atmosphere and land model am4. 0/LM4. 0: 2. Model description, sensitivity studies, and tuning strategies. *Journal of Advances in Modeling Earth Systems*, *10*(3), 735–769. https://doi.org/10.1002/2017ms001209